

Efficient estimation of error bounds for quantum multiparametric imaging with constraints

Alexander Mikhalychev,¹ Saif Almazrouei,² Svetlana Mikhalycheva,¹
Abdellatif Bouchalkha,² Dmitri Mogilevtsev,¹ and Bobomurat Ahmedov^{3,4}

¹*B.I. Stepanov Institute of Physics, NAS of Belarus, Nezavisimosti ave. 68-2, Minsk, Belarus**

²*Directed Energy Research Centre, Technology Innovation Institute, Abu Dhabi, United Arab Emirates*

³*Institute of Fundamental and Applied Research,
National Research University TIIAME, Kori Niyoziy 39, Tashkent 100000, Uzbekistan*

⁴*New Uzbekistan University, Movarounnahr str. 1, Tashkent 100000, Uzbekistan*

(Dated: December 13, 2024)

Advanced super-resolution imaging techniques require specific approaches for accurate and consistent estimation of the achievable spatial resolution. Fisher information supplied to Cramér-Rao bound (CRB) has proved to be a powerful and efficient tool for resolution analysis and optical setups optimization. However, the standard CRB is not applicable to constrained problems violating the unbiasedness condition, while such models are frequently encountered in quantum imaging of complex objects. Complimentary to the existing approaches based on modifying CRB, we propose a practical algorithm for approximate construction of a modified Fisher information matrix, which takes the constraints into account and can be supplied to the standard CRB. We demonstrate the efficiency of the proposed technique by applying it to 1-, 2-, and multi-parameter model problems in quantum imaging. The approach provides quantitative explanation of previous results with successful experimental reconstruction of objects with the spatial scale smaller than the theoretical limit predicted by the standard CRB.

Keywords: Quantum imaging, superresolution, Fisher information, constrained estimation

I. INTRODUCTION

The problem of diffraction limit of resolution in imaging was perceived and quantified more than a century ago [1, 2]. The first approaches to resolution quantification (such as Rayleigh criterion) were based on formalizing visual distinguishability of small features. While being intuitive and very fruitful in physics, the approach does not account, for example, for the influence of the shot noise on the image quality. Further, more advanced approaches based on Fourier components transfer were developed [3]. Recent progress in super-resolution imaging [4–7] forced the researchers to perceive the collected images (raw datasets) as quite abstract sources of information about the investigated sample rather than just visual replicas of it. Instead of measuring intensity of the light emitted or scattered by the sample, the super-resolution techniques are based on detection of photon coincidences [4, 8–11], analysis of time-dependent signal for fluctuating emitters [12–16], or scanning with localized excitation of fluorophors [17–19]. Since the resulting image is typically formed by elaborate processing of the raw information, the approaches to resolution quantification are to be tailored in the way suitable for taking that into account.

A powerful mathematical tool for quantification of the information content of various images (including both raw data and the processing results) is Fisher information (FI) [20]. It describes sensitivity of the measured

signal (or processed image) to variation of the sample parameters of interest. Cramér-Rao bound (CRB) [21, 22] connects FI with the errors of sample parameters' estimation for optimal analysis of the acquired signal. The approach has been successfully used for resolution analysis in quantum imaging of simple [23–27] and complex [24, 28] model objects, optimization of detection protocols [29–34], quantum light sources [28, 34], and cumulant order in super-resolution optical fluctuation imaging (SOFI) [35, 36]. Roughly speaking, resolution of a specific quantum or quantum-inspired imaging technique equals the smallest size of the sample details, such that the input signal (image) provides enough information for their reconstruction [34, 35].

Despite of strong success in applying classical and quantum FI to theoretical investigation of quantum imaging, direct exploitation of CRB has important limitations when constraints are imposed on the considered problem. In particular, the resolution experimentally achieved in Ref. [28] for multiparametric quantum imaging was several times better than the theoretical limit derived from CRB without accounting for constraints. Similar effect (reduction of the estimation variance) was previously reported for experiments [27] and numerical simulations [29, 37] for separation of two incoherent point-like light sources, as well as for resolution of a spectrometer [24].

The reason of those discrepancies is known from statistics [38–41] and consists in the unbiasedness assumption, which is used during derivation of CRB and, generally, becomes invalid when physical constraints are taken into account. For example, for a passive non-emitting object,

* mikhalychev@gmail.com

the absolute values of the transmission amplitude must belong to the range from 0 to 1. From physical point of view, constraints introduce additional *a priori* knowledge about the sample, complementary to the information provided by the detected signal, and enable reconstruction of smaller features. Mathematically, constraints typically lead to estimation bias [42], while biased estimators can ensure smaller mean square errors than unbiased ones [24, 39, 41, 43, 44].

Efficiency of CRB for resolution analysis on the one hand and typicality of constrained problems in practical imaging on the other hand make it tempting to reconcile them. One of the available approaches is based on constructing the modified CRB [38, 40, 41, 43], which explicitly takes the bias into account by incorporating its derivatives over the parameters of interest. Such approach has been successfully used for simple 1-parameter models in quantum imaging and metrology: estimation of the separation between 2 incoherent point sources [27, 29, 37] and inference of the wavelength by a spectrometer [24]. Minimization of the predicted estimation error over the bias allows to construct uniform (universal) version of CRB [45–47]. The resulting trade-off between the bias and the variance of the estimate can serve for resolution quantification in biomicroscopy [48–50]. While the approach is fruitful for derivation of general theoretical bounds on estimation errors, its practical application to quantifying information content of particular quantum imaging methods and setups can be cumbersome. Analytical calculation of neither bias gradient for a selected estimator, nor the optimal bias seems feasible for a real multiparametric problem of object reconstruction in quantum imaging [28], thus leading to the necessity of time-consuming numerical Monte-Carlo simulations.

In the present contribution we propose an alternative approach, which, instead of rigorous bounds, provides only an approximate assessment of the errors and resolution, but can be efficiently applied to multiparametric problems in practice. The essence of the method is to make use of the correspondence between FI and Bayesian probabilities [51, 52], to modify the probability distribution according to constraints as it was done previously in our paper on quantum tomography [53], and to map the new probability distribution back to FI. The modification of the probability distribution can be interpreted as taking the prior information encoded in the constraints into account. The resulting updated Fisher information matrix (FIM) already effectively includes the information about the constraints and induced estimation bias and can be put directly into the initial unmodified CRB. We apply the developed approach to multiparametric estimation problems in quantum imaging and show that it is capable of explaining and quantifying the resolution enhancement due to constraints experimentally observed in Ref. [28]. It is worth noting that the influence of the estimation bias on the predicted errors can be much more pronounced in quantum imaging based on measurement and analysis of photon coincidences (higher-order field

correlation functions) relatively to traditional intensity-based microscopy, because FI tends to become singular if the investigated object has dark (non-transmitting) areas. We pay special attention to that issue and show that the case is still covered by the proposed approach.

The rest of the paper is organized as follows. First, we briefly introduce the main concepts from estimation and probability theory useful for further derivation and analysis of the approach. Section III is devoted to constrained estimation problems and the core procedures of our paper: regularization and correction of FIM. In Section IV, we assess the efficiency and accuracy of the proposed approach by applying it to several model problems, ranging from very simple one to practical multiparametric imaging.

II. FISHER INFORMATION, PROBABILITIES, AND RESOLUTION

A. Fisher information

General purpose of measurements, including the ones used in imaging, is to estimate physical characteristics of the investigated system from the collected data [54]. For that purpose, one typically needs to construct the theoretical model of the signal $\mathbf{S}(\boldsymbol{\theta})$, where the vector $\boldsymbol{\theta} = \{\theta_\mu\}$ describes the parameters to be inferred from the experiment. Actually collected signal

$$\mathbf{Y} = \mathbf{S}(\boldsymbol{\theta}) + \boldsymbol{\varepsilon}, \quad (1)$$

inevitably contains noise contribution $\boldsymbol{\varepsilon}$ and, therefore, represents a particular realization of random variable(s). Statistical properties of the noise can be formalized by introduction of the likelihood $L(\mathbf{Y}|\mathbf{S})$.

The ability to reconstruct the parameters of interest from the measured data and the resulting inference error are determined by the *sensitivity* of the signal to the investigated parameters. The sensitivity can be quantified by the *score* function [20]:

$$s_\mu(\boldsymbol{\theta}) = \frac{\partial l(\mathbf{Y}|\mathbf{S}(\boldsymbol{\theta}))}{\partial \theta_\mu}, \quad (2)$$

where $l(\mathbf{Y}|\mathbf{S}(\boldsymbol{\theta})) = \log L(\mathbf{Y}|\mathbf{S}(\boldsymbol{\theta}))$ is the log-likelihood.

The covariance matrix of the score represents the Fisher information matrix (FIM) [20]:

$$\begin{aligned} F_{\mu\nu} &= \text{Cov}(s_\mu(\boldsymbol{\theta}), s_\nu(\boldsymbol{\theta})) \\ &= \text{E} \left(\frac{\partial l(\mathbf{Y}|\mathbf{S}(\boldsymbol{\theta}))}{\partial \theta_\mu} \frac{\partial l(\mathbf{Y}|\mathbf{S}(\boldsymbol{\theta}))}{\partial \theta_\nu} \right), \quad (3) \end{aligned}$$

where the symbol E denotes mathematical expectation over the distribution of the random signal \mathbf{Y} . Roughly speaking, larger values of the FIM elements correspond to more informative measurements.

The significance of FIM is enhanced by its usage in Cramér-Rao bound (CRB) [21, 22]. If the parameters

inference algorithm yields *unbiased* estimate $\hat{\boldsymbol{\theta}}$, i.e. its mathematical expectation equals the true value of the parameters: $E(\hat{\boldsymbol{\theta}}) = \boldsymbol{\theta}$, the covariance matrix of the estimated parameters is bounded from below by the inverse of the FIM:

$$\text{Cov}(\hat{\boldsymbol{\theta}}, \hat{\boldsymbol{\theta}}) \geq F^{-1}. \quad (4)$$

The matrix inequality $A \geq B$ means that the matrix $A - B$ is positive semidefinite.

Eq. (3) can be also rewritten as the expectation value of the log-likelihood curvature (see e.g. [54]):

$$F_{\mu\nu} = -E\left(\frac{\partial^2 l(\mathbf{Y}|\mathbf{S}(\boldsymbol{\theta}))}{\partial\theta_\mu\partial\theta_\nu}\right). \quad (5)$$

In the limit of high signal-to-noise ratio (SNR) typical for strong signals, that representation implies that FIM represents Hessian of maximum-likelihood estimate (MLE, formulated as finding $\hat{\boldsymbol{\theta}}$ maximizing the log-likelihood $l(\mathbf{Y}, \mathbf{S}(\hat{\boldsymbol{\theta}}))$ for the specific collected dataset \mathbf{Y}) and characterizes scattering of the estimation results for multiple repetitions of the experiment [52].

Alternatively, one can adhere to Bayesian approach [55] and consider posterior probability $p(\boldsymbol{\theta}|\mathbf{Y})$ of the parameters vector $\boldsymbol{\theta}$, conditioned by the measured dataset \mathbf{Y} . For a uniform prior probability distribution (absence of useful information about the investigated parameters before the measurement) and high SNR, the FIM F describes the shape of the posterior probability distribution near the point $\hat{\boldsymbol{\theta}}_{ML}$ of the likelihood maximum [51, 52]:

$$\begin{aligned} p(\boldsymbol{\theta}|\mathbf{Y}) &\propto L(\mathbf{Y}|\mathbf{S}(\boldsymbol{\theta})) \\ &\propto \exp\left[-\frac{1}{2}\left(\boldsymbol{\theta} - \hat{\boldsymbol{\theta}}_{ML}\right)^T F\left(\boldsymbol{\theta} - \hat{\boldsymbol{\theta}}_{ML}\right)\right]. \end{aligned} \quad (6)$$

The application of FI in terms of CRB is directly related to accuracy and resolution in imaging, while its Bayesian interpretation is helpful for our development of the constraints treatment approach. Some insights into relations between likelihood, distribution of point estimation results, and FI can also be gained from geometrical considerations presented in Appendix A.

It is also worth mentioning *quantum* Fisher information (QFI) [56–58], which generalizes the concept of classical FI and corresponds to the maximum of classical FI over all physically valid measurements. QFI represents a powerful tool for theoretical analysis of relatively simple systems [25, 26, 29, 30, 59–62] and can be applied even to practical multiparametric problems [63–65], but may require cumbersome calculations in that case. Due to the same structure and similar interpretation of classical FI and QFI, our approach remains applicable to QFI as well. However, in the current work we focus on practical applications considering quantum imaging with a fixed (not optimized) type of measurement and limit our analysis to classical FI.

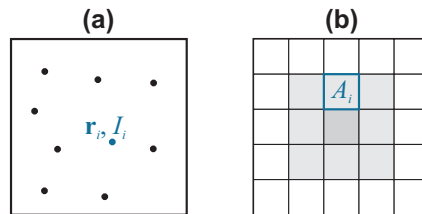


FIG. 1: Problem parameterization in quantum imaging: (a) by positions \mathbf{r}_i and brightnesses I_i of point emitters; (b) by transmission amplitudes A_i of pixels.

B. Fisher information in quantum imaging

In quantum imaging, the measured signal $\mathbf{S}(\boldsymbol{\theta})$ is typically represented by field correlation functions [4]

$$\begin{aligned} G^{(n)}(\mathbf{r}_1, t_1; \dots; \mathbf{r}_n, t_n) &= \left\langle E^{(-)}(\mathbf{r}_1, t_1) \dots E^{(-)}(\mathbf{r}_n, t_n) \right. \\ &\quad \left. \times E^{(+)}(\mathbf{r}_n, t_n) \dots E^{(+)}(\mathbf{r}_1, t_1) \right\rangle, \end{aligned} \quad (7)$$

where $E^{(\pm)}(\mathbf{r}, t)$ are positive(negative)-frequency field operators. Practically, the n -th order correlation function $G^{(n)}$ describes the rate of n -photon coincidence events for specified detection positions and time delays. If the main source of the detected signal fluctuations is the shot noise, the expression (3) can be simplified and takes the form (see, e.g. [30, 33, 34, 66]):

$$F_{\mu\nu} = \sum_i \frac{1}{S_i(\boldsymbol{\theta})} \frac{\partial S_i(\boldsymbol{\theta})}{\partial\theta_\mu} \frac{\partial S_i(\boldsymbol{\theta})}{\partial\theta_\nu}, \quad (8)$$

where $S_i(\boldsymbol{\theta})$ are components of the signal $\mathbf{S}(\boldsymbol{\theta})$, represented as a vector $\mathbf{S}(\boldsymbol{\theta}) = (S_1(\boldsymbol{\theta}), S_2(\boldsymbol{\theta}), \dots)$.

The set of inferred parameters $\boldsymbol{\theta}$ is determined by the model of the investigated object. In quantum imaging, the model is typically defined either as a set of discrete point emitters, parameterized by their positions \mathbf{r}_i and brightness I_i (Fig. 1(a)) [23–27, 29–33, 35, 64], or as a pixelized mask, characterized by the transmission amplitudes of the pixels A_i (Fig. 1(b)) [8–10, 28, 34, 67, 68].

FIM itself provides valuable information about the problem structure — parameters correlations and inaccuracies (see e.g. [26, 28, 65, 66]), since variance and covariances of the parameters are related to the inverse of FIM by CRB. For various optimization purposes, as well as for quantification of optical resolution, it is also useful to construct a scalar real-valued characteristic providing aggregate description of the accuracy in a multiparametric problem. There exist several common choices of such scalar quantity [69–72]: the volume of the joint confidence region defined by CRB (D -optimality — minimization of the determinant of the inverse of FIM: $\min \det F^{-1}$); the major axis of the joint confidence region (E -optimality — minimization of the maximal eigenvalue of the inverse of FIM: $\min \lambda_{max}(F^{-1})$); the perimeter of the enclosing box of the joint confidence

region (A -optimality — minimization of the trace of the inverse of FIM: $\min \text{Tr } F^{-1}$). The latter choice has already been applied to quantum imaging [28, 34, 35] by using the lower bound of total variance

$$\Delta^2 \equiv \text{Tr } F^{-1} \leq \sum_{\mu} \text{Var } \theta_{\mu} \quad (9)$$

as a measure of diffraction-caused inaccuracy.

FI represents a powerful and useful tool for resolution quantification in imaging. If inference of the positions (separation) of point emitters is considered, CRB directly provides a resolution measure: the predicted (minimal) inaccuracy of the position reconstruction quantifies the resolving power of the microscope [23–25, 27, 29, 31, 32]. For analysis of pixelized images, one can start from the notion that a feature is resolved if the acquired image (dataset) contains enough information for inference of the feature parameters with certain requested accuracy [23, 24, 34, 35]. In particular, one can define the spatial resolution as the minimal spatial scale of the problem (or feature size), for which the quantity defined by Eq. (9) is lower than certain threshold value determined by further exploitation purposes of the imaging results [34, 35]: $\Delta^2 \leq \Delta_{\text{threshold}}^2$.

The close connection of FI to achievable resolution allows to use it for optimization of the imaging setup. Increase of FI, including removal of “Rayleigh’s curse” in simple cases, indicated apparent advantages of detection protocols based on spatial modes demultiplexing [29, 30, 33, 73, 74], modification of point-spread function (PSF) [31, 32], or probabilistic transformation of an entangled light state [34]. Analysis of FI proved to be useful in optimization of quantum light sources [28, 34] and selection of the optimal cumulant order in super-resolution optical fluctuation imaging (SOFI) [35, 36].

In both object parameterizations discussed above, some basic constraints can limit the range of meaningful values for the parameters. For example, brightness of any emitter or the absolute value of the separation between two emitters should be non-negative ($I_i \geq 0$, $\Delta r \equiv |\mathbf{r}_1 - \mathbf{r}_2| \geq 0$). For a passive transmitting object, the absolute value of a pixel transmission amplitude cannot exceed 1: $|A_i| \leq 1$. In a commonly encountered case of an object with a real-valued transmission amplitude (see e.g. Refs. [8–11, 75–77]), the constraint takes the form

$$0 \leq A_i \leq 1. \quad (10)$$

A remarkable illustration of the constraints influence on the practically achievable spatial resolution was provided by the experiment reported in Ref. [28]. A number of pixelized objects (1-dimensional sets of slits and 2-dimensional masks) were illuminated by biphotons and pseudothermal light and the second- and third-order correlation functions were recorded. Quite unexpectedly, actually achieved resolution was several times higher than

the theoretical limit, predicted without taking the constraints into account. Namely, the resolution limit (minimal pixel size d_{min} defined from FI according to the predicted inference accuracy for the pixels’ transmission amplitudes [34]) was approximately a half of the Rayleigh limit d_R for the used optical system: $d_{\text{min}} \approx (0.4 \div 0.5)d_R$. The experimental datasets allowed successful object features reconstruction for the parameterization with a noticeably smaller pixel size: $d \approx (0.25 \div 0.28)d_R < d_{\text{min}}$.

Those counter-intuitive results were explained by a specific feature (still, quite common for model experiments) of the imaged objects: the actual transmission amplitude of their pixels took binary values $A_i = 0$ or 1. Therefore, the constraints (10) were active (i.e., influenced the reconstruction process) and provided additional information about the sample. It is worth noting, that the information about such binary type of the objects was not implied *a priori* and was not used to assist the reconstruction algorithm. The connection between the resolution enhancement and the constraints was verified by Monte-Carlo simulations and numerical estimation of the inference accuracy. The achievable resolution (minimal pixel size for reliable reconstruction of the transmission amplitudes) was approximately twice better for black-and-white model objects (with active constraints) than for the corresponding gray objects (when the constraints are inactive because the values are far from 0 and 1). However, a way to quantitative theoretical FI-based prediction of such resolution improvement was not considered in Ref. [28]. In the current contribution, we aim to fill that gap.

III. CONSTRAINED ESTIMATION AND FISHER INFORMATION

A. Influence of constraints on parameter estimation

When the estimation formalism is applied to real-world tasks, the true values of the parameter may be constrained by a specific physical domain: $\boldsymbol{\theta} \in \Omega$. In that case, it is reasonable to impose the constraints on the estimated values as well: $\hat{\boldsymbol{\theta}} \in \Omega$. If the constraints are active (i.e., the true values of the parameters are within the estimation inaccuracy from the boundaries of the region Ω), the relation between FI and the estimation errors becomes more complicated than prescribed by CRB (Eq. (4)). The constrained estimation typically violates unbiasedness condition [42], required for validity of CRB.

In Bayesian treatment of the problem, the constraints induce nontrivial prior probability: $p_0(\boldsymbol{\theta}) = 1/|\Omega|$ for $\boldsymbol{\theta} \in \Omega$ and 0 otherwise. Since prior probabilities are not taken into account by FI, it does not describe the posterior probability by Eq. (6) correctly for constraint problems.

The influence of the constraints on the distribution of estimated parameter values in 1-parameter case is shown

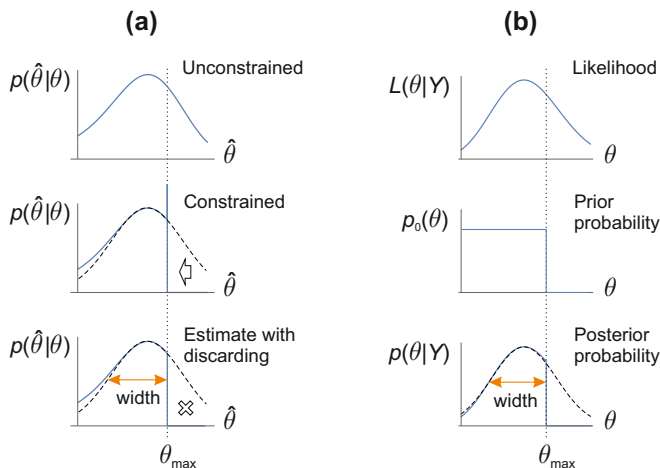


FIG. 2: Influence of a constraint $\theta \leq \theta_{\max}$ on the estimate distribution: (a) distribution of the estimated parameter value $\hat{\theta}$ for its true value θ (from top to bottom — unconstrained estimate, constrained estimate, and formally introduced estimate with discarded nonphysical values); (b) Bayesian posterior probability for the parameter θ for a given signal value Y (from top to bottom — unconstrained likelihood, prior probability distribution describing the constraint, and the resulting posterior probability). Dashed lines show Gaussian fit of the unconstrained distributions. The resulting width after the constraint application is smaller than the one predicted by FI.

in Fig. 2 (provided just as an illustration without connection to any specific physical model). It is worth noting, that Bayesian “cutting” of the posterior probability distribution by setting zero prior probability for nonphysical values can be formally reproduced in the distribution of point estimation results by performing unconstrained estimation and subsequent discarding of nonphysical values $\hat{\theta}_{\text{unconstr.}} \notin \Omega$. In high-SNR case, the resulting distributions will have practically the same width. While that estimate with the values discarding does not follow typical practical procedures of parameter inference, it is useful for getting some insights for the development of the FIM modification approach.

In 1-parameter case, the constraint-induced decrease of the parameter reconstruction error (the width of the estimate distribution) is quite limited. Taking into account that the true value $\theta \in \Omega$ belongs to the physical domain and assuming that the distribution $p(\hat{\theta}|\theta)$ is symmetric around the true value θ , one can easily see that the width is minimal for θ having a boundary value ($\theta = \theta_{\max}$ for the case shown in Fig. 2) and reaches 1/2 of the initial width of the unconstrained distribution. The effect can be much more pronounced for a multi-parameter problem [28]. Fig. 3 illustrates the statement for a model 2-parameter problem, where the error is reduced by the factor of approximately 6.

B. Effective Fisher information matrix for constrained estimation

For unconstrained problems, FIM can be used for efficient prediction of experimental inference inaccuracies via CRB (Eq. (4)). In high-SNR regime, FIM also represents the quadratic form kernel for Gaussian approximation of the estimated parameters distribution (Eq. (6)). Mathematically, the two meanings of FIM are ensured by the relation between the quadratic form and the covariance matrix of a multivariate normal distribution:

$$p(\hat{\theta}) \propto \exp \left[-\frac{1}{2} \Delta \hat{\theta}^T F \Delta \hat{\theta} \right] \Rightarrow \text{Cov}(\hat{\theta}, \hat{\theta}) = F^{-1}, \quad (11)$$

where $\Delta \hat{\theta} = \hat{\theta} - E(\hat{\theta})$.

When the constraints are applied to the problem, the basic CRB becomes invalid (due to bias of the estimate) while usage of its modified versions [38, 40, 41, 43] is typically computationally expensive. On the other hand, transformation of probability distributions $p(\hat{\theta}) \mapsto p_{\text{constr.}}(\hat{\theta})$ caused by application of the constraints is quite straightforward, as discussed above.

From practical point of view, one is interested in errors of the parameters estimation, namely in the covariance matrix $\text{Cov}_{\text{constr.}}(\hat{\theta}, \hat{\theta})$ for the constrained distribution. If the distribution $p_{\text{constr.}}(\hat{\theta})$ can be approximated by a multivariate normal distribution $\tilde{p}(\hat{\theta})$, the relation similar to Eq. (11) will hold:

$$\tilde{p}(\hat{\theta}) \propto \exp \left[-\frac{1}{2} \Delta \hat{\theta}^T \tilde{F} \Delta \hat{\theta} \right] \Rightarrow \text{Cov}_{\text{constr.}}(\hat{\theta}, \hat{\theta}) \approx \tilde{F}^{-1}, \quad (12)$$

where $\Delta \hat{\theta} = \hat{\theta} - E_{\text{constr.}}(\hat{\theta})$. The quadratic form \tilde{F} of the probability distribution $\tilde{p}(\hat{\theta})$ can be interpreted as the FIM for the constrained problem and quantifies the error of constrained parameters estimation via usual (unmodified) CRB defined by Eq. (4). The transition from the initial FIM F to the modified FIM \tilde{F} is shown schematically in Fig. 4. Since the proposed procedure of FIM modification preserves the form of CRB for constrained problems, further analysis methods based on CRB (e.g., quantification of resolution [34] or optimization of the measurement setup [28]) remain valid.

Computationally efficient procedure of transforming $p(\hat{\theta})$ into $\tilde{p}(\hat{\theta})$ has been proposed in Ref. [53] in the connection with adaptive quantum tomography with Bayesian update of the knowledge about the analyzed quantum state. The constraints are assumed to be linear and have the form $\mathbf{a}_j^T \boldsymbol{\theta} \leq b_j$. The idea of the approach consists in iterative shrinking of the probability distribution according to the current most severely violated constraint.

Let the probability distribution obtained after the i -th iteration be described as

$$p^{(i)}(\hat{\theta}) \propto \exp \left[-\frac{1}{2} \Delta \boldsymbol{\theta}^T F^{(i)} \Delta \boldsymbol{\theta} \right], \quad \Delta \boldsymbol{\theta} = \hat{\boldsymbol{\theta}} - \boldsymbol{\theta}^{(i)}. \quad (13)$$

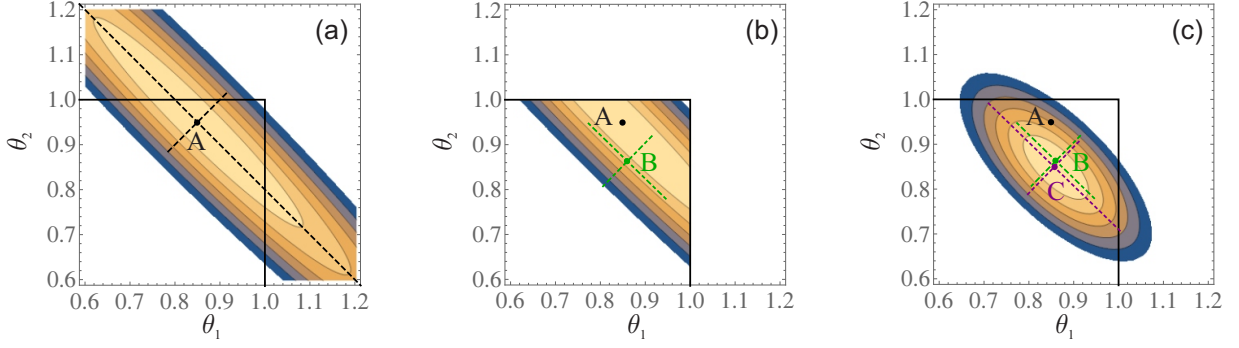


FIG. 3: Influence of constraints $\theta_1 \leq 1$ and $\theta_2 \leq 1$ on the distribution of parameters' estimates for a model 2-parameter case: probability distribution for an unconstrained problem (a), constrained distribution corresponding to posterior probability for Bayesian treatment or to the formal distribution of the estimated parameters values after discarding nonphysical results (b), and Gaussian approximation of the constrained distribution according to Subsection III B (c). Capital letters A, B, and C indicate the mean values for the probability distributions shown in panels (a), (b), and (c) respectively. Dashed lines correspond to the eigenvectors of the covariance matrix and indicate the corresponding widths of the distributions. The constrained estimate is biased (the point B is shifted from the point A indicating the true values of the parameters θ_1 and θ_2). Errors of the parameters' estimation become approximately 6 times smaller when the physical constraints are taken into account.

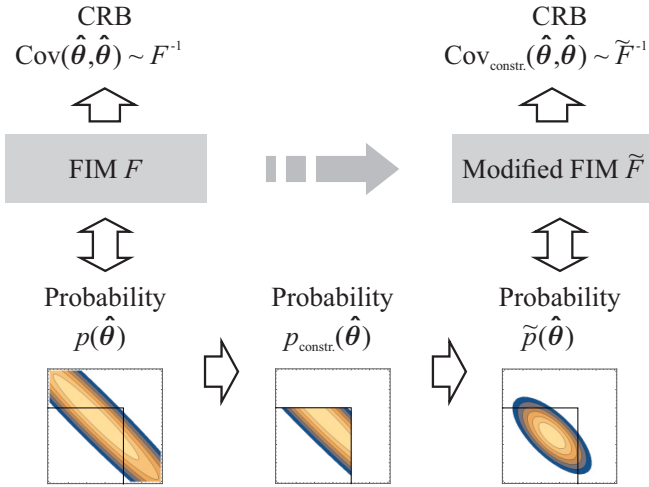


FIG. 4: Scheme of taking constraints into account by construction of modified FIM. The basic FIM F corresponds to the unconstrained problem and, in high-SNR regime, represents the quadratic form kernel for the probability distribution $p(\hat{\theta})$ of unconstrained parameter estimates. Then, the constraints are applied to the probability distribution and the result is approximated by a multivariate normal distribution $\tilde{p}(\hat{\theta})$. The kernel \tilde{F} of that distribution's quadratic form can be interpreted as the modified FIM since it is related to the covariance of the constrained parameter estimates through usual CRB.

Then, the $(i + 1)$ -th iteration transforms $p^{(i)}(\hat{\theta})$ into $p^{(i+1)}(\hat{\theta})$ and includes the following steps [53] (see Appendix B for a visual illustration and additional expressions):

- Construct a matrix $T = T^T = (F^{(i)})^{1/2}$ and apply a linear coordinate transformation $\hat{\theta} \mapsto \theta' = T(\hat{\theta} - \theta^{(i)})$, such that the transformed distribution has zero mean $\theta^{(i)'} = 0$ and the quadratic form kernel represented by the unit matrix: $F^{(i)'} = T^{-1}F^{(i)}T^{-1} = 1$. The transformation is non-degenerate, if $F^{(i)}$ is not singular.
- Recalculate all the constraints to the new coordinates as $\mathbf{a}_j \mapsto \mathbf{a}'_j = \mathbf{a}_j T^{-1}$, $b_j \mapsto b'_j = b_j - \mathbf{a}_j^T \theta^{(i)}$.
- Find the index of the most severely violated constraint: $j = \text{argmin}_j (b'_j / |\mathbf{a}'_j|)$.
- Shrink the distribution in the direction $\mathbf{d} = \mathbf{a}'_j / |\mathbf{a}'_j|$ corresponding to the found constraint: $F^{(i)'} \mapsto F^{(i)''} + \xi \mathbf{d} \mathbf{d}^T$, $\theta^{(i)'} \mapsto \theta^{(i)''} = -\delta \mathbf{d}$. Explicit expressions for δ and ξ are listed in Appendix B.
- Apply the inverse transform to get the resulting probability distribution after the current iteration: $F^{(i+1)} = T F^{(i)''} T = F^{(i)} + \xi T \mathbf{d} \mathbf{d}^T T$, $\theta^{(i+1)} = \theta^{(i)} - \delta T^{-1} \mathbf{d}$.

C. Ill-defined Fisher information matrix for dark objects

Both, application of CRB (4) to the unmodified FIM and implementation of the proposed iterative correction require FIM to be non-singular in order to get meaningful results. However, multi-parameter estimation problem in quantum imaging can yield an ill-defined FIM if the object contains a dark (non-transparent) region.

In particular, for a uniform object with the transmission amplitude A , the n -th order correlation function $G^{(n)}$, defined by Eq. (7), is polynomial relatively to A : $G^{(n)} \propto A^{2n}$. Then, FI, calculated for the problem parameter A , scales as $F \propto A^{2(n-1)}$. For conventional intensity-based imaging ($n = 1$), the singularity is absent: $2(n-1) = 0$ and F remains non-zero for $A = 0$. However, for detection of correlation functions with $n \geq 2$, one has $F = 0$ for $A = 0$ (quite similarly to ‘‘Rayleigh’s curse’’ for inference of two point light sources separation [29]).

As another illustrative example of quantum imaging, one can consider illumination of the object by ideally correlated biphotons. The second-order correlation function can be represented as [4]

$$G^{(2)}(\mathbf{r}_1, \mathbf{r}_2) \propto |\Psi(\mathbf{r}_1, \mathbf{r}_2)|^2 \equiv \left| \int d^2\mathbf{s} A^2(\mathbf{s}) h(\mathbf{s}, \mathbf{r}_1) h(\mathbf{s}, \mathbf{r}_2) \right|^2 \quad (14)$$

where $A(\mathbf{s})$ is the transmission amplitude of the object at the point with the transverse position \mathbf{s} , and $h(\mathbf{s}, \mathbf{r})$ is the PSF (Green’s function) of the optical system. For a pixelized object and an array detector, the second order correlation between the i -th and j -th pixels of the detector can be expressed as [28]

$$G_{ij}^{(2)} \propto |\Psi_{ij}|^2 = \left| \sum_m D_m^{(ij)} A_m^2 \right|^2 \quad (15)$$

with certain coefficients $D_m^{(ij)}$ (real-valued for simple models [28]). According to Eq. (8), diagonal elements of FIM are proportional to

$$F_{mm} \propto A_m^2 \sum_{i,j} \left(D_m^{(ij)} \right)^2 \propto A_m^2. \quad (16)$$

for the considered parameterization. Therefore, the adverse scaling of FIM for $A_m \rightarrow 0$ remains the same as for the toy example of a uniform object.

D. Regularization of ill-defined Fisher information matrix

An insight to the reasons of FIM singularity and inapplicability of CRB for quantum imaging of dark objects can be gained from Eqs. (5) and (6). Roughly speaking, the local properties of the log-likelihood, characterized by its second derivative over the parameters, are used to estimate the distribution shape and to quantify its width. However, such local properties can be non-representative if the distribution shape is far from the assumed one.

To assist our intuition, it is worth considering a simple problem resembling the discussed behavior of FI. Let us suppose we are given a profile $y(x)$ with the maximum at $x = 0$ and need to estimate the width of that peak. If the peak has Gaussian shape ($y(x) \propto e^{-x^2/(2\sigma^2)}$), the

half-width σ can be estimated by calculating the second derivative of the profile logarithm:

$$\sigma = \frac{1}{\sqrt{|Y^{(2)}(0)|}}, \quad Y^{(2)}(x) \equiv \frac{d^2}{dx^2} (\log y). \quad (17)$$

Now, let us consider the profiles $y_1 = e^{-\max(0, (|x-x_0|)^2/(2\sigma^2))}$ and $y_2 = e^{-|x|^k/(2\sigma^k)}$, $k > 2$ (Fig. 5(a)). In both cases, we have $Y^{(2)}(0) = 0$ and Eq. (17) is inapplicable for estimation of σ , while the actual width remains finite. To get meaningful width estimates, one can probe the slope of the peak by calculating $Y^{(2)}(x')$ for shifted positions $x' \neq 0$ and construct the quantities

$$\Delta(x') = |x'| + \sigma(x') \equiv |x'| + |Y^{(2)}(x')|^{-1/2}. \quad (18)$$

Geometrically, we fit different parts of the peak slope by a Gaussian-shape peak and estimate the resulting width (Fig. 5(b)). For the profile $y_1(x)$, the value

$$\sigma_{\min} = \min_{x'} \Delta(x') \quad (19)$$

will be exactly the half-width of the peak (Fig. 5(b)). For the function $y_2(x)$, Eq. (19) provides an approximate result, which, however, is still quite accurate (see Fig. 5(c) and Appendix C).

One should treat the discussed illustrative example with caution: the toy example deals with a continuous dependence $y(x)$, while the actually detected signal \mathbf{Y} in quantum imaging typically represents a vector of discrete integer-valued random variables. Moreover, it is the discreteness of the detected signal that leads to singularity of FIM for a dark object (Appendix D). Still, the gained insights can be used for regularization of FIM.

To design the regularization procedure for FIM, we start from considering 1-parameter case. When the error Δ of estimating the parameter θ is analyzed on the base of CRB, FI $F(\theta)$ (which, in the case of a single parameter, is a scalar — 1×1 matrix) plays the role similar to the quantity $Y^{(2)}(x)$, introduced in Eq. (17):

$$\Delta \sim \frac{1}{\sqrt{F(\theta)}}. \quad (20)$$

That analogy is also supported by definition of FIM according to Eq. (5).

In the case of a dark object ($F \approx 0$), Eq. (20) strongly overestimates the error, since the second derivative is not representative enough for the probability distribution shape. Following the idea of Eqs. (18) and (19), one can define

$$\Delta(\theta') = |\theta' - \theta| + F^{-1/2}(\theta') \quad (21)$$

and estimate the inaccuracy as

$$\Delta_{\min} = \min_{\theta'} \Delta(\theta'). \quad (22)$$

The approach is illustrated by Fig. 11 in Appendix A.

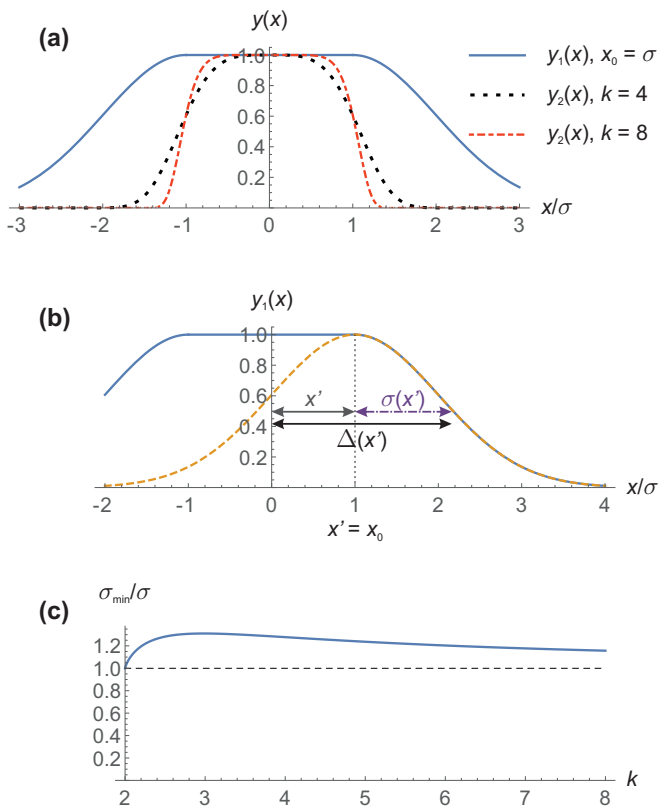


FIG. 5: Width estimation by the second derivative. (a) Model profiles defined in the text (blue solid line — $y_1(x)$ with $x_0 = \sigma$; black dotted line — $y_2(x)$ with $k = 4$; red dashed line — $y_2(x)$ with $k = 8$). (b) Width estimation by “scanning” the profile by a Gaussian-shape peak: total half-width $\Delta(x')$ includes the half-width $\sigma(x')$ estimated at the shifted position x' and the displacement x' . (c) Half-width estimate σ_{\min} for $y_2(x)$ according to the proposed approach normalized by the true half-width σ of the profile (at the height $e^{-1/2}$).

Now, we aim at constructing a modified FI $\tilde{F}(\theta)$ such that the initial form of the relation $\Delta = \Delta_{\min} \sim 1/\sqrt{\tilde{F}(\theta)}$ holds. This requirement can be fulfilled by defining

$$\tilde{F}(\theta) = \frac{1}{\Delta_{\min}^2} = \max_{\theta'} \frac{F(\theta')}{(1 + |\theta' - \theta| \sqrt{F(\theta')})^2}. \quad (23)$$

In a general multi-parameter case, one can apply the discussed regularization along main axes of FIM independently. If FIM $F(\boldsymbol{\theta})$ is decomposed as

$$F(\boldsymbol{\theta}) = \sum_i \lambda_i \mathbf{v}_i \mathbf{v}_i^T, \quad (24)$$

where λ_i and \mathbf{v}_i are eigenvalues and eigenvectors respectively, and $\mathbf{v}_i^T \mathbf{v}_j = \delta_{ij}$, one can consider the shifts $\boldsymbol{\theta}' = \boldsymbol{\theta} + \mathbf{v}_i \delta\theta$ for each separate direction \mathbf{v}_i . The direct analog of the scalar FI $F(\theta')$ for 1-parameter case is

the projection of FIM for the shifted parameters at the considered direction:

$$\lambda_i(\delta\theta) = \mathbf{v}_i^T F(\boldsymbol{\theta} + \mathbf{v}_i \delta\theta) \mathbf{v}_i. \quad (25)$$

Therefore, the generalization of Eq. (23) to the multi-parameter case is

$$\tilde{F}(\boldsymbol{\theta}) = \sum_i \tilde{\lambda}_i \mathbf{v}_i \mathbf{v}_i^T \quad (26)$$

where

$$\tilde{\lambda}_i = \max_{\delta\theta} \frac{\lambda_i(\delta\theta)}{(1 + |\delta\theta| \sqrt{\lambda_i(\delta\theta)})^2}. \quad (27)$$

It is worth noting that we neither provide accurate proof of the proposed regularization procedure nor claim that the constructed modified FIM $\tilde{F}(\boldsymbol{\theta})$ ensures a rigorous bound via CRB for the estimation error. Rather, the approach is expected to be a useful practical tool for approximate assessment of the errors and resolution for multiparametric problems in quantum imaging. The next section illustrates the approach with several examples, starting from a simple 1-parameter toy example and covering resolution estimation in practical multiparametric quantum imaging.

IV. APPLICATION OF THE APPROACH TO QUANTUM IMAGING

A. One-parameter model

To illustrate the proposed procedures of FIM correction for constrained problems in quantum imaging and assess the accuracy of the approach, we start from a simple toy example of a uniform object with the transmission amplitude A , $0 \leq A \leq 1$, representing the only parameter of interest. Let us assume that the light source emits groups of n time-correlated photons and the n -photon coincidence events are detected. For $n = 2$, such process corresponds to emission of biphotons by spontaneous parametric down-conversion (SPDC) in a nonlinear crystal. Let the number of the emitted photon groups per an experiment have the mean value N and be described by Poisson distribution. Then, the detected signal Y has the expectation value

$$S(A) = N\eta^n A^{2n}, \quad (28)$$

where η is the light collection efficiency.

The likelihood for the signal Y (taking integer values) corresponds to Poisson distribution:

$$L(Y|S(A)) = \frac{S^Y(A)}{Y!} e^{-S(A)}. \quad (29)$$

Eq. (8) for FIM is applicable in the considered case and yields the result

$$F(A) = 4n^2 N \eta^n A^{2(n-1)}. \quad (30)$$

As references for evaluation of the proposed approach, we consider the following two estimates of the transmission amplitude A :

- Constrained MLE:

$$\begin{aligned} \hat{A}_{\text{MLE}}(Y) &= \operatorname{argmax}_{0 \leq A' \leq 1} L(Y|S(A')) = \min(1, S^{-1}(Y)) \\ &= \min(1, Y^{1/(2n)} N^{-1/(2n)} \eta^{-1/2}). \end{aligned} \quad (31)$$

- Mean over posterior probability distribution according to Bayes' formula:

$$\hat{A}_{\text{B}}(Y) = \frac{\int_0^1 dA' L(Y|S(A')) A'}{\int_0^1 dA' L(Y|S(A'))}. \quad (32)$$

It is worth noting that the latter one also represents the optimal biased estimate (following the spirit of Refs. [43, 44, 47]), minimizing the mean squared error (MSE) averaged over the range of the true values $A \in [0, 1]$ (Appendix E 1).

Fig. 6(a) shows the bias of the estimates \hat{A}_{MLE} and \hat{A}_{B} for $N = 200$, $\eta = 0.7$, $n = 2$. One can see that the estimates are, indeed, biased near the boundary values $A = 0$ and $A = 1$ (in the regions I and III respectively).

Fig. 6(b) shows the dependence of the estimation error

$$\Delta = \sqrt{\text{MSE}} = \sqrt{\text{E}[(\hat{A} - A)^2]} \quad (33)$$

on the true value A of the transmission amplitude for the two estimators (blue and orange lines correspond to MLE and Bayesian estimators respectively). For each estimator, the MSE is calculated directly from the probability distribution (solid colored lines) and from modified CRB taking the bias into account [43] (dashed colored lines). One can notice that in the region I the error strongly depends on the estimator used; changing the bias, one can “redistribute” the inaccuracy over the range of the parameter A [41]. Still, the error remains finite for the whole range $A \in [0, 1]$. The details of the calculations are described in Appendix E 2.

Black lines in Fig. 6(b) correspond to application of basic CRB (namely, Eq. (20)) to the unmodified FI $F(A)$ (solid black line), FI after regularization according to Eq. (23) (dotted black line; see Appendix E 3), and FI $\tilde{F}(A)$ regularized and then corrected for the constraints (dot-dashed black line; see Appendix E 4). The regularization procedure resolves the divergence of the basic CRB with unmodified FI at $A = 0$. The correction, described in Subsection III B, further improves the error estimate and makes it consistent with the actual inaccuracies indicated by the colored lines in Fig. 6(b) (up to the strong variation of the error for different estimators in the region I).

B. Two-parameter model

As the next step of the proposed procedure illustration, we consider the following two-parameter model. The object

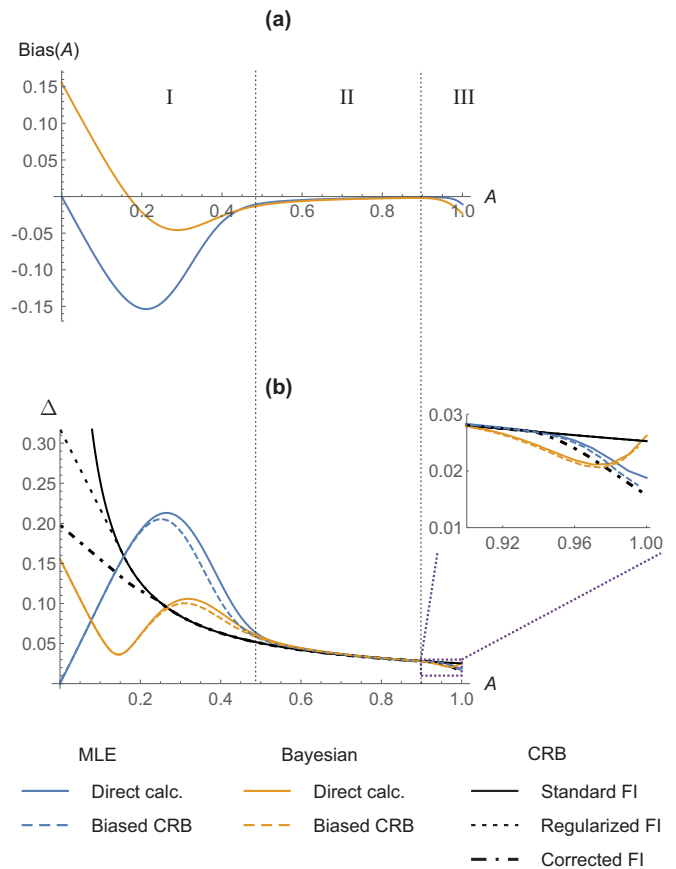


FIG. 6: Transmission amplitude estimation for a uniform object (single-parameter model): estimation bias (a) and error (b). The notations of line styles are listed in the text. The regions I and III correspond to biased estimates for dark (A close to 0) and bright (A close to 1) objects respectively. In region II, the value A is far from the boundaries and the estimate is almost unbiased. The inset in panel (b) shows a zoomed-in part of the region III, where the constraint $A \leq 1$ leads to the estimation bias.

consists of two parts with the transmission amplitudes A_1 and A_2 , representing the parameters of interest: $\boldsymbol{\theta} \equiv \mathbf{A} = (A_1, A_2)$. The physical domain of the parameters' values is naturally defined as $\Omega = \{\mathbf{A} | 0 \leq A_i \leq 1\}$. We assume that the object is illuminated by an SPDC light source, producing in average N photon pairs ($n = 2$) per an experiment, and the second-order autocorrelations are measured by a pair of detectors with the efficiency η . The signal vector $\mathbf{S}(\mathbf{A})$ contains two components, which are described according to Eq. (15) as

$$S_i(\mathbf{A}) = N\eta^2 G_{ii}^{(2)} = N\eta^2 \left| \sum_{m=1,2} D_m^{(ii)} A_m^2 \right|^2, \quad i = 1, 2. \quad (34)$$

For simplicity, we assume that the coefficients $D_m^{(ii)}$ are

real and symmetric:

$$D_m^{(ii)} \in \mathcal{R}, D_1^{(11)} = D_2^{(22)} = h_0, D_2^{(11)} = D_1^{(22)} = h_1. \quad (35)$$

Therefore, the signal components can be expressed as

$$S_1(\mathbf{A}) = N\eta^2 (h_0 A_1^2 + h_1 A_2^2)^2, \quad (36)$$

$$S_2(\mathbf{A}) = N\eta^2 (h_1 A_1^2 + h_0 A_2^2)^2. \quad (37)$$

The realizations of the measured signal $\mathbf{Y} = (Y_1, Y_2)$ are assumed to be characterized by Poisson distribution with Y_i having the expectation value $S_i(\mathbf{A})$. The FIM for the problem can be calculated according to Eq. (8) and equals

$$F(\mathbf{A}) = 16N\eta^2 (h_0^2 + h_1^2) \begin{pmatrix} A_1^2 & \zeta A_1 A_2 \\ \zeta A_1 A_2 & A_2^2 \end{pmatrix}, \quad (38)$$

where

$$\zeta = \frac{2h_0 h_1}{h_0^2 + h_1^2}, \quad |\zeta| < 1 \text{ for } h_0 \neq h_1. \quad (39)$$

For comparison with the error prediction by the proposed approach, we consider the following estimates of the parameters of interest \mathbf{A} :

- Constrained MLE:

$$\hat{\mathbf{A}}_{\text{MLE}}(\mathbf{Y}) = \underset{\mathbf{A}' \in \Omega}{\operatorname{argmax}} [L(\mathbf{Y}|\mathbf{S}(\mathbf{A}'))] \quad (40)$$

where the 2-component likelihood is factorized into two single-component likelihood functions $L(\mathbf{Y}|\mathbf{S}(\mathbf{A}')) = L(Y_1|S_1(\mathbf{A}'))L(Y_2|S_2(\mathbf{A}'))$, which are defined by Eq. (29).

- Bayesian mean *a posteriori* estimate:

$$\hat{\mathbf{A}}_{\text{B}}(\mathbf{Y}) = \frac{\int_0^1 dA'_1 \int_0^1 dA'_2 L(\mathbf{Y}|\mathbf{S}(\mathbf{A}')) \mathbf{A}'}{\int_0^1 dA'_1 \int_0^1 dA'_2 L(\mathbf{Y}|\mathbf{S}(\mathbf{A}'))}. \quad (41)$$

Fig. 7 shows the results for the considered 2-parameter model. The estimators listed above are applied to 1000 random samples of the signal \mathbf{Y} for the true values of the transmission amplitudes localized in the lower part (a), the center (b), and the upper part (c) of the physical domain. The estimation results $\mathbf{Y} \mapsto \hat{\mathbf{A}}$ are shown as points in each part of the figure. The statistics of each generated dataset is shown as an ellipse, indicating the mean value $\langle \hat{\mathbf{A}} \rangle$ and the covariance $C = \operatorname{Cov}(\hat{\mathbf{A}}, \hat{\mathbf{A}})$ according to the approach described in Appendix F:

$$\Delta \mathbf{A}^T C^{-1} \Delta \mathbf{A} = 2 \log 2, \quad \Delta \mathbf{A} = \mathbf{A} - \langle \hat{\mathbf{A}} \rangle. \quad (42)$$

The results of random sampling are compared with the error predictions based on CRB and FIM: the standard one $F(\mathbf{A})$, calculated according to Eq. (38), and the FIM $\tilde{F}(\mathbf{A})$ obtained by applying the proposed regularization

and correction procedures to $F(\mathbf{A})$. The FIMs $F(\mathbf{A})$ and $\tilde{F}(\mathbf{A})$ are also visualized as ellipses (Appendix F).

First, one can notice that in the case, shown in Fig. 7(b), the true value $\mathbf{A} = (0.5, 0.5)$ is far from the boundaries. The regularization and correction procedures act trivially: $\tilde{F}(\mathbf{A}) = F(\mathbf{A})$ and the dashed and solid black ellipses coincide. The statistics of MLE and Bayesian estimates almost coincide with each other and with the prediction according to CRB (still, some estimation bias is present).

For the cases when the constraints are active (Fig. 7(a,c)), CRB with standard FIM strongly overestimates the errors. The sampling statistics depends on the particular estimator used. Up to that variability, the corrected FIM provides a reasonable prediction of the parameters estimation inaccuracies.

C. Practical multiparametric models in quantum imaging

To conclude testing of the proposed approach, we apply it to multiparametric quantum imaging problems analyzed in Refs. [28, 34]. The considered imaging setup is schematically shown in Fig. 8(a) and follows the ideas of the biphoton imaging experiment in Ref. [28]. An object consists of vertical slits (each having width d and a constant transmission amplitude — Fig. 8(b)) and is illuminated by entangled photon pairs. The radiation is collected by an optical system with the resolution limit d_{R} (classical Rayleigh limit for incoherent imaging). The registered signal represents coincidence counts number for a pair of detectors.

First, we consider a 10-parameter model with the object shown in Fig. 8(b) [34] and parameterized by the transmission amplitudes A_m (each describing the region $(m-1)d \leq x \leq md$ of the object): $\boldsymbol{\theta} \equiv \mathbf{A} = (A_1, \dots, A_{10})$. We choose $A_{\text{min}} = 0.9$ for testing the correction-only procedure and $A_{\text{min}} = 0$ as the case when both regularization and correction of FIM are required.

The incident photon pairs are assumed to be ideally correlated, and the signal is described by Eq. (15) with $i = j$ and the sampling points corresponding to the step $d/2$ in the object plane:

$$S_j(\mathbf{A}) = NG^{(2)}(x_j, x_j) = N \left| \sum_m D_m^{(jj)} A_m^2 \right|^2, \quad (43)$$

where N is the expectation value of the total number of detected coincidence events (already taking into account the detectors efficiency), $x_j = jd/2$,

$$D_m^{(jj)} = 4k_{\text{max}}^2 \int_{(m-1)d}^{md} ds \operatorname{sinc}^2 [k_{\text{max}}(s - x_j)], \quad (44)$$

and $k_{\text{max}} = 3.83/d_{\text{R}}$ is the momentum transfer cut-off of the optical system [34].

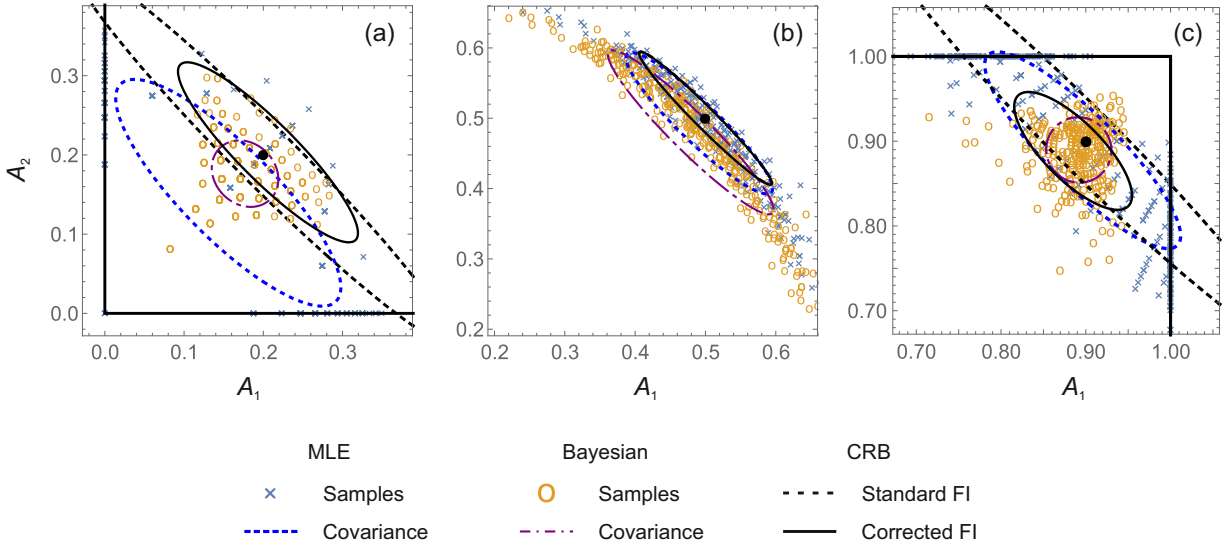


FIG. 7: Transmission amplitudes estimation for the 2-parameter model. The true parameters values are $A_1 = A_2 = 0.2$ (a), 0.5 (b), and 0.9 (c), as indicated by black dots. Blue crosses and orange circles show the parameter inference results of a randomly sampled signal for MLE and Bayesian estimate respectively. 1000 samples were used for statistics estimation; 300 samples are shown in the figure; some results coincide due to discreteness of the signal. The modeling parameters are $\eta = 0.7$, $h_0 = 1$, $h_1 = 0.8$; $N = 1000$ (a,b) and 50 (c). Ellipses (blue dotted for MLE and purple dot-dashed for Bayesian estimate) are centered at the mean of the sampled results and have the shape defined by the corresponding covariance matrix (Appendix F). Black dotted ellipse (extending beyond the plotted regions) shows the predicted results scattering according to CRB with the standard FIM $F(\mathbf{A})$. Black solid ellipse corresponds to the regularized and corrected FIM $\tilde{F}(\mathbf{A})$. Straight black lines show the constraints imposed on the parameters A_1 and A_2 .

Similarly to previous examples, Poisson statistics of the signal is assumed, and the FIM is calculated according to Eq. (8). The total value of the estimation error, predicted by CRB, can be quantified by the quantity Δ^2 defined in Eq. (9) and applied to both the standard FIM $F(\mathbf{A})$ and its regularized and corrected counterpart $\tilde{F}(\mathbf{A})$. As a reference for quality assessment of the predictions, we also perform direct estimation of the transmission amplitudes $\hat{\mathbf{A}}$ for the signal \mathbf{Y} randomly sampled according to its likelihood $L(\mathbf{Y}|\mathbf{S}(\mathbf{A}))$. The inference is performed by minimizing the distance between the realized signal \mathbf{Y} and its parameterized expectation value $\mathbf{S}(\hat{\mathbf{A}})$:

$$\hat{\mathbf{A}} = \underset{\mathbf{A}'}{\operatorname{argmin}} |\mathbf{Y} - \mathbf{S}(\mathbf{A}')|^2. \quad (45)$$

The estimation inaccuracy is characterized by the total variance and MSE for the sampling results:

$$\Delta_{\text{Var}}^2 = \sum_m \operatorname{Var}(\hat{A}_m), \quad \Delta_{\text{MSE}}^2 = \langle |\hat{\mathbf{A}} - \mathbf{A}|^2 \rangle. \quad (46)$$

Fig. 8(c) shows the dependence of the estimation error Δ^2 on the spatial scale of the problem d/d_R for the model object presented in Fig 8(b) with $A_{\min} = 0.9$. The number of the detected coincidence events is taken to be $N = 10^4$. The error Δ^2 calculated for the standard FIM $F(\mathbf{A})$ (solid line) accurately describes the variance for

unconstrained estimation (red star-marked points). If the constraint $0 \leq A_m \leq 1$ is imposed during the transmission amplitudes inference according to Eq. (45), the variance (green circles) and MSE (purple crosses) become smaller. Such error decrease is accurately reproduced by using CRB with the corrected FIM $\tilde{F}(\mathbf{A})$ (dashed blue line).

Fig. 8(d) presents similar results for the case $A_{\min} = 0$, which requires regularization of FIM. Application of CRB to the standard FIM does not yield meaningful results in that case since $F(\mathbf{A})$ is singular. For that reason, only the constrained estimation was sampled and compared to the error prediction by the regularized and corrected FIM $\tilde{F}(\mathbf{A})$. One can see that the agreement between the results of the proposed approach and direct sampling is good.

As the last example, we consider the object from a model quantum imaging experiment presented in Ref. [28]. The spatial resolution, achieved in practice, was higher than the theoretical bound predicted by CRB with the standard FIM. Such counter-intuitive result in Ref. [28] was the motivation for the current research. The measurement setup in the discussed experiment corresponded to the scheme in Fig. 8(a). The resolution of the optical system was artificially worsened by decreasing the numerical aperture for demonstration of sub-Rayleigh imaging and corresponded to the Rayleigh limit

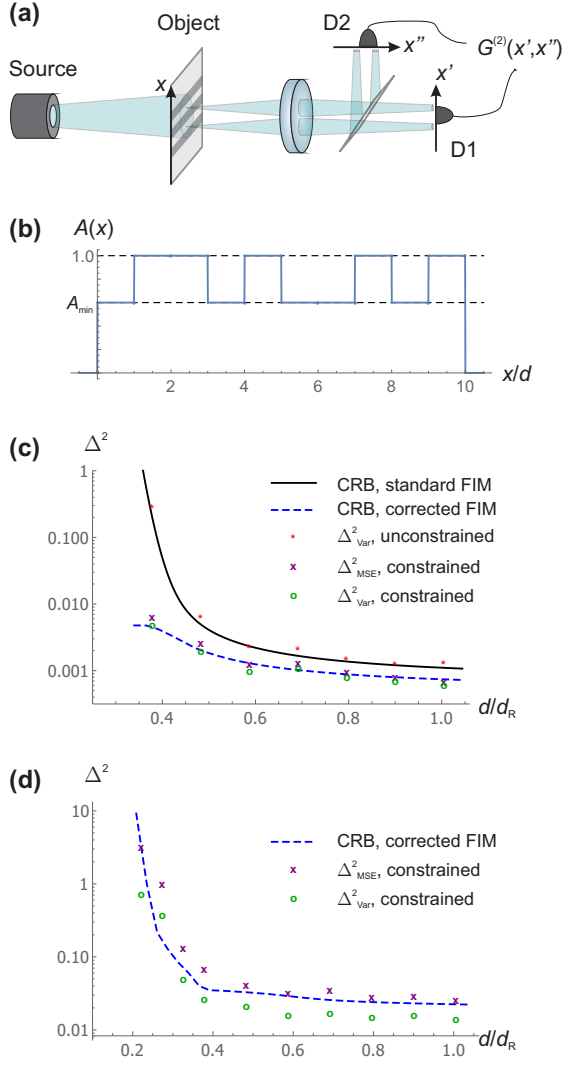


FIG. 8: Transmission amplitudes estimation for the 10-parameter model. (a) Scheme of the modeled imaging setup. Biphoton radiation, passing through the investigated object, is collected by an optical system and split between two single-photon detectors. The signal is represented by the correlation function $G^{(2)}(x', x'')$ depending on the detectors' positions x' and x'' . (b) Transmission amplitude of the model object as a function of the transverse coordinate x normalized by the width d of the slits (extended pixels) used for pixelation of the object. (c,d) The dependence of the estimation error on the slit width d normalized by the Rayleigh resolution limit d_R for $A_{\min} = 0.9$ (c) and $A_{\min} = 0$ (d). The notations and line styles are described in the text.

$d_R = 30.0 \mu\text{m}$. In contrast to the previous idealized 10-parameter imaging model, the spatial correlation of biphotons is not assumed to be ideal here (i.e., the photons from a pair have non-zero probability of passing through different parts of the object).

The object is shown in Fig. 9(a). Physically, it rep-

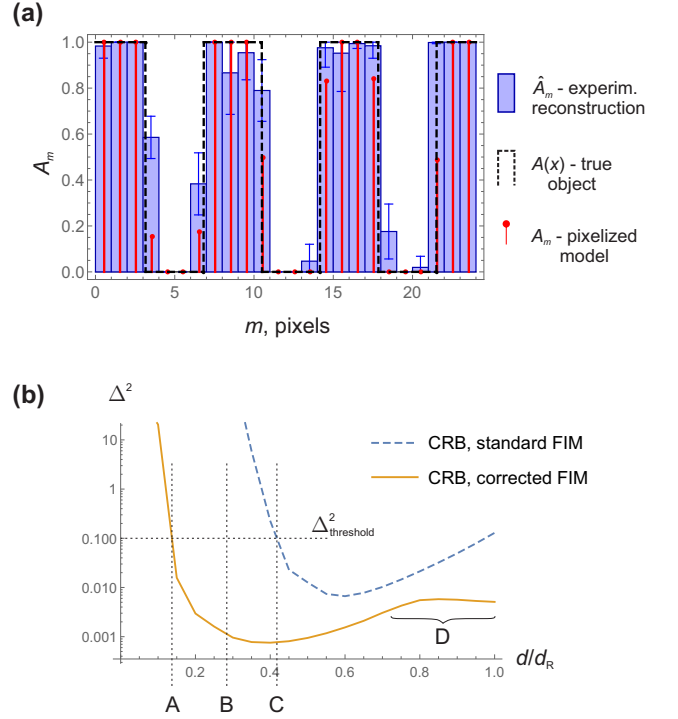


FIG. 9: Transmission amplitudes estimation for the 24-parameter model from Ref. [28]. (a) Transmission amplitude of the model object: pixelized reconstruction result $\hat{\mathbf{A}} = \{\hat{A}_m\}$ from Ref. [28] (filled blue rectangles) with error bars built on the base of repeated measurement results; true transmission amplitude of the model object $A(x)$ (dashed black line); and its pixelized counterpart representing the true values $\mathbf{A} = \{A_m\}$ of the parameters of interest for the solved problem (red vertical bars). (b) The dependence of the estimation error on the slit width d normalized by the Rayleigh resolution limit d_R via CRB with the standard FIM (dashed blue line) and the regularized and corrected FIM (solid orange line). The dotted vertical lines indicate characteristic resolution values: A — the resolution limit for the corrected FIM, defined for the threshold error value $\Delta^2_{\text{threshold}} = 0.1$; B — the spatial scale of the successful experimental inference of the object transmission amplitude [28]; C — the resolution limit for the standard FIM. In region D, the regularizing effect of the non-ideal biphoton correlations decreases with the growth of the problem scale d .

resents 3 non-transparent (dark) slits on a transparent background (a part of a positive USAF 1951 resolution target) with the slit width $31.25 \mu\text{m}$. For statement of the estimation problem, the object was divided into 24 slit-like pixels and parameterized by 24 values of the transmission amplitude $\theta \equiv \mathbf{A} = (A_1, \dots, A_{24})$. The true values \mathbf{A} used for our modeling (Fig. 9(a)) corresponded to the actual object used in the experiment [28].

The measured signal $\mathbf{S}(\mathbf{A})$ is represented by the full correlation matrix $G^{(2)}(x_i, x_j)$ without the constraint $i =$

j [28]:

$$S_{ij}(\mathbf{A}) = NG^{(2)}(x_i, x_j) = N \left| \sum_{m,l} D_{ml}^{(ij)} A_m A_l \right|^2 \quad (47)$$

where the expressions for calculation of the coefficients $D_{ml}^{(ij)}$ are provided in Ref. [28], and N is the expectation value of the total number of detected coincidence events. As previously, we assume independent Poissonian statistics for the components Y_{ij} of the measured signal \mathbf{Y} . Therefore, FIM is described by Eq. (8) and takes the form

$$F_{ml}(\mathbf{A}) = 4N \sum_{i,j} \left(\sum_{l'} D_{ij}^{(ml')} A_{l'} \right) \left(\sum_{m'} D_{ij}^{(m'l)} A_{m'} \right). \quad (48)$$

Typically, it is sufficient to have at least one non-dark pixel ($\exists l : A_l \neq 0$) to ensure non-zero values of the expressions in parentheses and, therefore, non-singular FIM $F(\mathbf{A})$. The non-ideal biphoton correlations produce regularizing effect by shifting the problem closer to coherent light imaging, where the FIM singularity issue does not arise.

Fig. 9(b) shows the results of resolution estimation via CRB for $N = 10^5$. The total reconstruction error Δ^2 , defined by Eq. (9), is calculated for the standard FIM $F(\mathbf{A})$ (dashed blue line) and the regularized and corrected one $\tilde{F}(\mathbf{A})$ according to the proposed approach (solid orange line). The achievable resolution can be defined as the minimal problem scale (pixel size) $d = d_{\min}$, for which the reconstruction error Δ^2 remains within certain reasonable limit: $\Delta^2 \leq \Delta_{\text{threshold}}^2$ [34]. For illustration purposes, the threshold value $\Delta_{\text{threshold}}^2 = 0.1$, consistent with the actual experimental noise in Ref. [28], is used in Fig. 9(b). For such selection of the threshold, the theoretical resolution limit for the standard FIM is $d_{\min}/d_R \approx 0.42$, which is larger than the spatial scale $d/d_R = 8.51 \mu\text{m}/30.0 \mu\text{m} = 0.28$ of the problem, successfully solved experimentally [28]. FIM correction according to the proposed approach shifts the resolution limit to the value $d_{\min}/d_R \approx 0.14$, thus, resolving the seeming contradiction of beating the ultimate theoretical limit experimentally.

An interesting and rather counter-intuitive feature of the obtained dependencies is the growth of the predicted error Δ^2 when the spacial scale d of the problem increases (region D). The effect is closely related to the regularizing influence of the finite transverse correlation length of non-ideal biphotons, discussed after Eq. (48). When the pixel size increases and the correlation length remains constant, the cross-term coefficients $D_{ml}^{(ij)}$ with $m \neq l$ tend to zero and the standard FIM becomes ill-defined. However, the effect is less pronounced for the regularized and corrected version of FIM.

V. CONCLUSIONS

A priori constraints, imposed on quantum imaging problems, can improve stability of the object parameters inference and decrease the errors beyond the CRB-based theoretical limit (strictly speaking, inapplicable due to estimation bias). The approach, proposed in the current paper, restores the applicability of the usual form CRB to such constrained problems by constructing a modified FIM, which includes the constraints and is regularized if the initial (standard) FIM turns out to be ill-defined.

The proposed FIM correction and regularization technique represents a practical tool suitable for complex multiparametric models and accurate enough to be used for resolution analysis. A competitive approach, based on modified CRB [43, 47], requires knowledge of the bias derivatives, which may be infeasible for analytical calculation and very time-consuming for estimation by numerical Monte-Carlo simulations. Even for a relatively simple 2-parameter case, the analytical description of biased constrained estimates is cumbersome.

The proposed approach was successfully applied to 1-, 2-, 10-, and 24-parameter imaging problems and exhibited a good agreement with other methods of error estimation. For the simplest 1-parameter model, it is possible to describe various estimators and to quantify resolution analytically. Many fundamental theoretical works have already been devoted to such simple models. For 2 parameters, it is still possible to estimate the errors directly, but the calculations are more complicated. When a multiparametric problem is considered, the proposed procedure continues to work well and yields meaningful results, while other approaches require huge computational efforts. In particular, the developed technique of FIM modification helped us to explain the high resolution achieved experimentally in Ref. [28] and to predict the resolution limit for such a constrained problem quantitatively. It is worth noting that the applicability of the developed approach can be extended to problems with a larger number of parameters (e.g., hundreds or thousands) by analyzing sub-problems of a reasonable size after splitting the initial problem into almost independent windows [28].

The ability to construct the modified FIM for constrained problems can be useful for resolution estimation (as shown in the last considered example), problem structure analysis (similar to the one performed in Ref. [28], but more accurate for constrained problems), imaging setup optimization, and other similar tasks. The applicability of the approach extends far beyond quantum optics. For example, Monte-Carlo simulations for high-resolution X-ray diffraction in Ref. [66] demonstrated decrease of the estimation variance when the natural physical constraints imposed on the parameters of interest became active. The proposed technique is capable of predicting such effect on the base of the modified FIM and CRB.

Since QFI equals the classical FI for the optimal mea-

surement, it is affected by the *a priori* constraints in a very similar way. Therefore, the developed approach is not limited to classical FI, and can be applied to QFI as well.

ACKNOWLEDGMENTS

A.M., S.M., and D.M. acknowledge support from the National Academy of Sciences of Belarus program “Convergence”. A.M. and S.M. acknowledge partial support from BRFFR grant F24KI-058 and from MSHE-RF grant 075-15-2024-556. A.M. and D.M. also acknowledge partial support from BRFFR grant F23UZB-064.

Appendix A: Geometry of likelihood and Fisher information

The close connection of FI with distribution of the estimation results (via CRB) on the one hand and with the likelihood (via the definition (3)) on the other hand gives rise to its frequentist and Bayesian interpretations (see e.g. Refs. [51, 52]). Geometry of the connection between the likelihood, distribution of the estimation results, and FI is illustrated by Fig. 10. The maps schematically represent the likelihood $L(Y|\theta)$ for a simple 1-parameter problem with a scalar (1-dimensional) signal Y .

Fig. 10(a) corresponds to interpretation of FI in terms of the estimation results distribution for a fixed model. If the true value of the parameter equals θ , the possible realizations of the detected signal Y are distributed according to the likelihood $L(Y|\theta)$, shown in the inset (a') for specific θ and representing the vertical cross section AB of the map. Inference of the investigated parameter through its MLE $\hat{\theta}$ corresponds to processing the detected signal value Y by mapping $Y \mapsto \hat{\theta} = \operatorname{argmax}_{\hat{\theta}} L(Y|\hat{\theta})$. Geometrically, each point of the segment AB is mapped onto the curve CD. The resulting distribution $p(\hat{\theta}|\theta)$, shown in the inset (a''), describes frequencies of getting the estimated values $\hat{\theta}$ in a detection-inference procedure if the true value of the investigated parameter equals θ . In the high-SNR limit, the distribution can be approximated by a Gaussian profile (dashed line in inset (a'')). The width of the distribution (total length $l(CA) + l(BD)$ of the segments CA and BD) characterizes the estimation error and is determined by FI.

The geometry for the Bayesian interpretation of FI is illustrated in Fig. 10(b). For a given value of the measured signal Y , the posterior distribution $p(\theta|Y)$ of the parameter θ (inset (b')) represents a horizontal cross-section EF of the likelihood map. In the high-SNR limit, the Gaussian approximation of the posterior probability is valid (dashed line in the inset (b')), with it width $l(EF)$ determined by the FI according to Eq. (6).

By overlaying the segment EF onto the plot in Fig. 10(a), one can see that, in the high-SNR limit, the

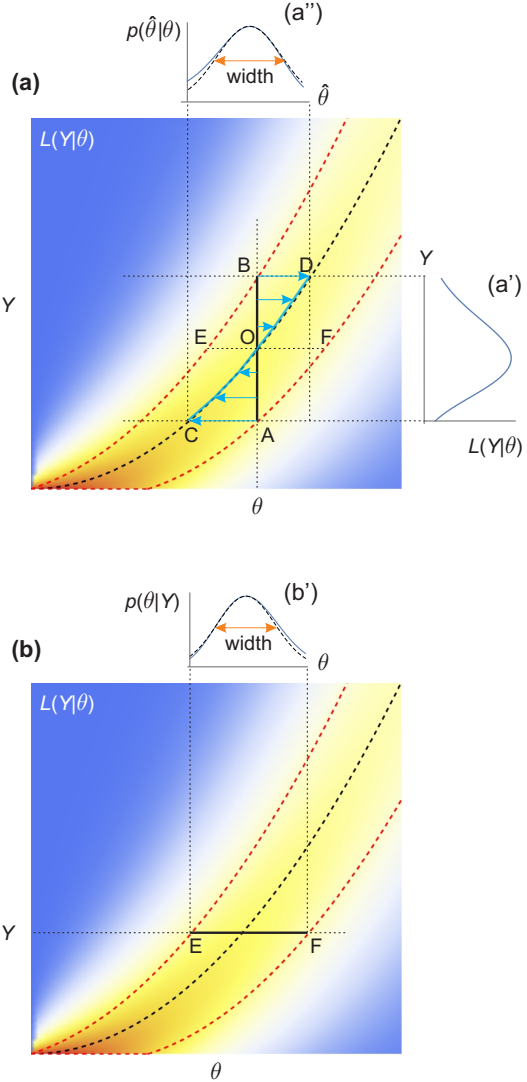


FIG. 10: Geometry of likelihood and FI: (a) distribution of the estimated parameter value $\hat{\theta}$ for a given true value θ of the parameter; (b) Bayesian posterior probability for the parameter θ for a given signal value Y . The details are provided in the text of Appendix A. The segment EF is also shown in panel (a) for the purpose of comparing the two interpretations. For simplicity, the signal Y is shown as a continuous variable, while for quantum-optical measurements it is typically a discrete variable taking integer values (the number of detected photons or coincidence events).

two interpretations of the FI lead to the same predicted error (width of the probability distribution). In that limit, the curve CD is almost a straight line. Therefore, the shapes EOB and OBD, as well as COA and AOF are close to triangles, which are equal to each other pairwise. The width $l(EF)$ of the posterior probability distribution in Bayesian interpretation is approximately the same as the deviation between the estimated and the true values

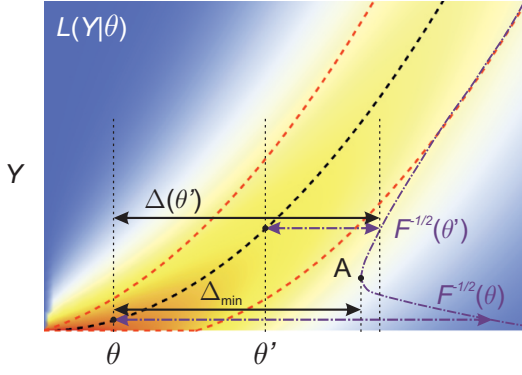


FIG. 11: FI regularization for 1-parameter problem.

The same likelihood diagram as in Fig. 10 is used. Purple dot-dashed line schematically shows the error estimate (upper bound for $\hat{\theta}$) based on FI (Eq. (20)), which diverges at $\theta \rightarrow 0$. The modified error estimate $\Delta(\theta')$ defined by Eq. (21) takes into account FI-based error estimate and the displacement $\theta' - \theta$ for a shifted parameter value θ' . The resulting regularized error estimate Δ_{\min} for θ is constructed by minimizing the quantity $\Delta(\theta')$ over θ' (Eq. (22) — i.e., by finding the rightmost point A along the purple dot-dashed curve).

of the parameter in the frequentist approach:

$$l(\text{EF}) = l(\text{EO}) + l(\text{OF}) \approx l(\text{BD}) + l(\text{CA}). \quad (\text{A1})$$

The introduced geometrical treatment of the likelihood and FI is also useful for illustration of the regularization procedure described by Eqs. (21) and (22) in Subsection III D — Fig. 11.

Appendix B: Iterative algorithm of Fisher information matrix modification

The iterative procedure of shrinking the multivariate normal probability distribution to fit certain linear constraints, described in Subsection III B of the main text, is illustrated by Fig. 12. The modification of the probability distribution follows the ideas from Ref. [53], but with certain changes discussed below.

After the coordinate transformation at the i -th iteration, one ends up with the probability distribution

$$p^{(i)}(\boldsymbol{\theta}') \propto \exp\left[-\frac{1}{2}(\boldsymbol{\theta}')^T \boldsymbol{\theta}'\right]. \quad (\text{B1})$$

For the k -th constraint $(\mathbf{a}'_k)^T \boldsymbol{\theta}' \leq b'_k$, one can define the probability of its violation

$$P_k = \int_{(\mathbf{a}'_k)^T \boldsymbol{\theta}' > b'_k} p^{(i)}(\boldsymbol{\theta}') d\boldsymbol{\theta}' = \frac{1}{2} \left[1 - \operatorname{erf}\left(\frac{b'_k}{\sqrt{2}|\mathbf{a}'_k|}\right) \right]. \quad (\text{B2})$$

The index of the most severely violated constraint is defined as

$$j = \operatorname{argmax}_k P_k = \operatorname{argmin}_k \frac{b'_k}{|\mathbf{a}'_k|}. \quad (\text{B3})$$

If the maximal probability of constraint violation P_j is smaller than certain threshold value (0.01 for the presented numerical calculations), the iterations are stopped and the probability distribution $p^{(i)}(\boldsymbol{\theta})$ is treated as the final result. Otherwise, one can introduce the variable $x = \mathbf{d}^T \boldsymbol{\theta}'$ (where $\mathbf{d} = \mathbf{a}'_j/|\mathbf{a}'_j|$), use the symmetry of the distribution (B1), and consider the marginal distribution $w'(x) \propto \exp(-x^2/2)$ with the constraint $x \leq x_0 \equiv b'_j/|\mathbf{a}'_j|$. Then, the considered iteration modifies the marginal distribution as

$$w'(x) \mapsto w''(x) \propto \exp\left[-\frac{1+\xi}{2}(x+\delta)^2\right] \quad (\text{B4})$$

with the parameters ξ and δ being chosen according to the following requirements:

- The probability of the constraint violation should be reduced by certain quantity η (small enough to ensure convergence of iterations — $\eta = 0.1$ for the presented numerical calculations): $P_j \mapsto P'_j = \max(P_j/2, P_j - \eta)$:

$$P'_j = \frac{1}{2} \left[1 - \operatorname{erf}\left(\frac{(x_0 + \delta)\sqrt{1+\xi}}{\sqrt{2}}\right) \right]. \quad (\text{B5})$$

- The width of the distribution in the prescribed domain $x \leq x_0$ should be preserved:

$$\operatorname{Var}(x|w'(x), x \leq x_0) = \operatorname{Var}(x|w''(x), x \leq x_0). \quad (\text{B6})$$

The latter requirement differs from the one considered in Ref. [53], where preservation of the mean value $\operatorname{E}(x|w'(x), x \leq x_0) = \operatorname{E}(x|w''(x), x \leq x_0)$ was more appropriate for the quantum state reconstruction task.

The two listed requirements imply the following expressions for the quantities ξ and δ :

$$\xi = \frac{V(P'_j, x'_0)}{V(P_j, x_0)} - 1, \quad (\text{B7})$$

$$\delta = \frac{x'_0}{\sqrt{1+\xi}} - x_0, \quad (\text{B8})$$

where $x'_0 = \sqrt{2} \operatorname{erf}^{-1}(1 - 2P'_j)$ and

$$V(p, x) = 1 - \frac{x e^{-x^2/2}}{\sqrt{2\pi}(1-p)} - \frac{e^{-x^2}}{2\pi(1-p)^2}. \quad (\text{B9})$$

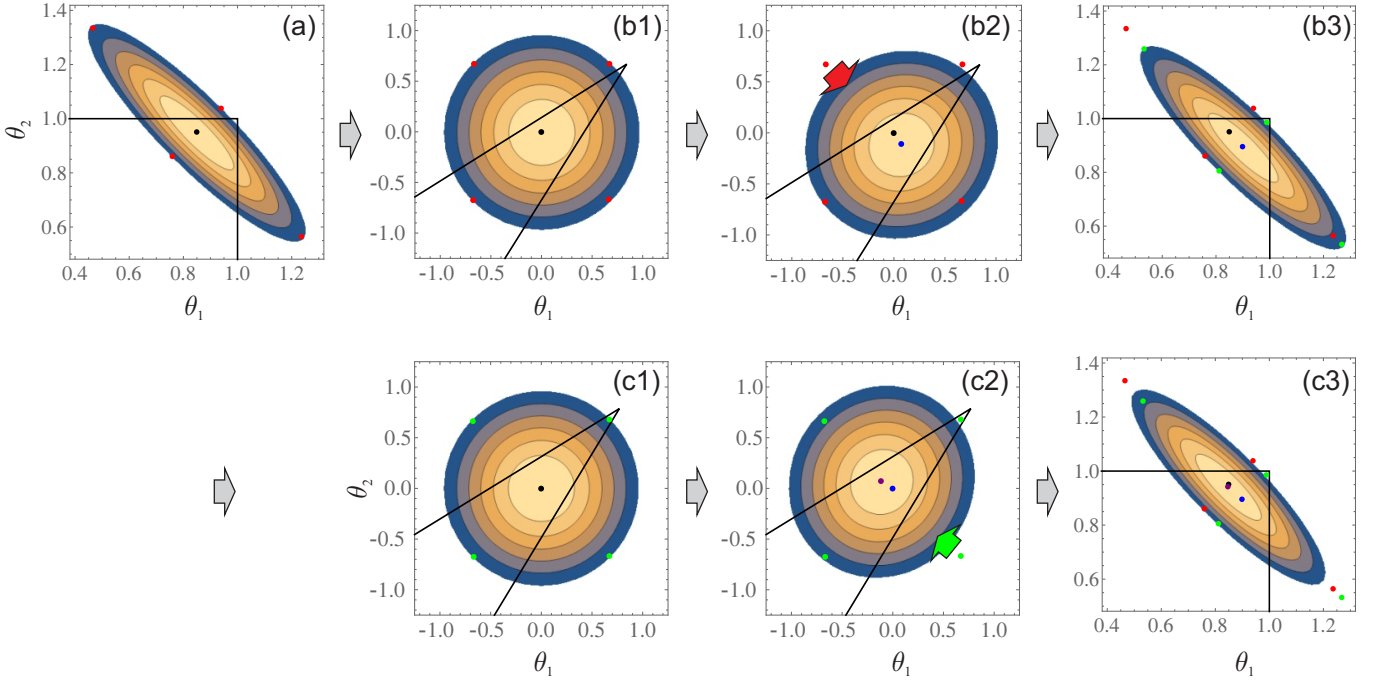


FIG. 12: Iterative shrinking of a model probability distribution in 2-parameter case: initial distribution (a) and two subsequent iterations (b1–b3) and (c1–c3). The constraints are $\theta_1 \leq 1$ and $\theta_2 \leq 1$. The black dot indicates the true values of the parameters $(\theta_1, \theta_2) = (0.85, 0.95)$. Each iteration starts from the coordinate transformation described in the Subsection III B of the main text (b1, c1). Then, the resulting distribution is modified to reduce the probability of violating one of the constraints (b2, c2). Finally, the inverse coordinate transform is applied (b3, c3). Red and green points indicate the shape of the probability distribution before the first and the second iterations respectively. Blue and purple points show the mean values for the modified distributions after the first and the second iterations respectively.

Appendix C: Examples of width estimation by the second derivative with regularization

For the model profile $y_1(x)$, defined in the main text, the second derivative of the logarithm takes the values

$$Y^{(2)}(x') = \begin{cases} 0 & \text{for } |x'| < x_0 \\ 1/\sigma^2 & \text{for } |x'| \geq x_0 \end{cases} \quad (\text{C1})$$

Therefore, according to the definition (18), $\Delta(x') \rightarrow \infty$ for $x' < x_0$ and $\Delta(x') = |x'| + \sigma$ otherwise. The minimum of $\Delta(x')$ is reached at $x' = \pm x_0$ and yields the accurate estimate of the half-width

$$\sigma_{\min} = x_0 + \sigma. \quad (\text{C2})$$

For the profile $y_2(x)$, the quantity $Y^{(2)}(x')$ equals

$$Y^{(2)}(x') = -\frac{k(k-1)|x'|^{k-2}}{2\sigma^k}. \quad (\text{C3})$$

The displaced half-width $\Delta(x')$, defined by Eq. (18) is equal to

$$\Delta(x') = |x'| + \sqrt{\frac{2\sigma^k}{k(k-1)}} |x'|^{1-k/2} \quad (\text{C4})$$

and reaches the minimal value at

$$x' = \pm \left[\frac{(k-2)^2}{2k(k-1)} \right]^{1/k} \sigma. \quad (\text{C5})$$

The resulting half-width estimate is

$$\sigma_{\min} = \left[\frac{(k-2)^2}{2k(k-1)} \right]^{1/k} \frac{k}{k-2} \sigma. \quad (\text{C6})$$

The dependence of the ratio σ_{\min}/σ on k is shown in Fig. 5.

Appendix D: Fisher information for 1-parameter problem with discrete and continuous signal

Here, we show that discreteness of the detected signal strongly influences the behavior of FI for dark objects. For simplicity, the 1-parameter model for a uniform object with the transmission amplitude A is considered and the mean value of the detected signal is assumed to scale as $S(A) \propto A^{2n}$.

First, let us consider the typical case, when the detected signal Y takes integer values distributed according

to the Poisson distribution with the mean $S(A)$:

$$L_P(Y|S(A)) = \frac{S^Y(A)}{Y!} e^{-S(A)}. \quad (\text{D1})$$

According to Eq. (8), the FI equals

$$F_P = \frac{1}{S(A)} \left(\frac{dS(A)}{dA} \right)^2 \propto A^{2(n-1)}. \quad (\text{D2})$$

Now, let us approximate the Poisson distribution by a continuous-variable Gaussian distribution with the same mean and variance:

$$L_G(Y|S(A)) = \frac{1}{\sqrt{2\pi S(A)}} \exp\left(-\frac{(Y-S(A))^2}{2S(A)}\right). \quad (\text{D3})$$

Then, FI can be calculated as

$$\begin{aligned} F_G &= \int_{-\infty}^{\infty} dY \frac{1}{L(Y|S(A))} \left(\frac{dL(Y|S(A))}{dA} \right)^2 \\ &= \left(\frac{1}{S(A)} + \frac{1}{2S^2(A)} \right) \left(\frac{dS(A)}{dA} \right)^2 \end{aligned} \quad (\text{D4})$$

In the limit of strong signal (bright object) $S(A) \gg 1$, the two noise distributions yield the same FI: $F_G \approx F_P$. However, for weak signal (dark object), the asymptotics is different:

$$F_G \sim \frac{1}{2S^2(A)} \left(\frac{dS(A)}{dA} \right)^2 \propto A^{-2} \rightarrow \infty \quad (\text{D5})$$

while $F_P \rightarrow 0$ for $A \rightarrow 0$ and $n > 1$.

Appendix E: Calculations for 1-parameter problem of transmission amplitude estimation

1. Optimal biased estimate

Optimizing the bias of a parameter estimate, one can reduce the MSE of the parameter relatively to unbiased estimates [41, 43, 44, 47]. For the model, described in Subsection IV A, one can specify the cost function for the bias optimization as the MSE averaged over the whole physical range of the true parameter values $A \in [0, 1]$:

$$\langle \Delta^2 \rangle_A \equiv \int_0^1 dA \mathbb{E}[(\hat{A}(Y) - A)^2] \quad (\text{E1})$$

where $\hat{A}(Y)$ is the estimator to be optimized, and the expectation value over the signal realization is defined as

$$\mathbb{E}[f(Y)] = \sum_{Y=0}^{\infty} L(Y|S(A)) f(Y). \quad (\text{E2})$$

Substituting Eq. (E2) into Eq. (E1), one can obtain the following expression for the cost function:

$$\begin{aligned} \langle \Delta^2 \rangle_A &= \sum_{Y=0}^{\infty} \left[\langle L(Y|S(A)) \rangle_A \hat{A}^2(Y) \right. \\ &\quad \left. - 2 \langle L(Y|S(A)) A \rangle_A \hat{A}(Y) + \langle L(Y|S(A) A^2) \rangle_A \right], \end{aligned} \quad (\text{E3})$$

where the brackets $\langle \dots \rangle$ denote averaging over A as in Eq. (E1). The optimization is performed over the discrete set of variables $\hat{A}(Y)$, parameterized by an integer index Y :

$$\frac{\partial}{\partial \hat{A}(Y)} \langle \Delta^2 \rangle_A = 0 \text{ for all } Y = 0, 1, \dots \quad (\text{E4})$$

The minimum is reached when the following equation is satisfied:

$$\hat{A}(Y) = \frac{\langle L(Y|S(A)) A \rangle_A}{\langle L(Y|S(A)) \rangle_A} = \frac{\int_0^1 dA' L(Y|S(A')) A'}{\int_0^1 dA' L(Y|S(A'))}. \quad (\text{E5})$$

The result coincides with the mean *a posteriori* estimate defined by Eq. (32).

2. Mean squared error estimation

For numerical analysis of the estimation error in 1-parameter case, one can start from constructing the mapping dictionary $Y \mapsto \hat{A}(Y)$ for the considered estimate. Eqs. (31) and (32) are to be used for MLE and Bayesian estimates defined in the main text. Then, the MSE and the bias are calculated as functions of the true parameter value A as

$$\text{MSE}(A) = \mathbb{E}[(\hat{A}(Y) - A)^2], \quad \text{Bias}(A) = \mathbb{E}[\hat{A}(Y) - A], \quad (\text{E6})$$

where the expectation value is defined by Eq. (E2).

FI-based error evaluation includes application of standard CRB ($\text{Var}(A) \sim 1/F$), modified CRB for a biased estimator [41, 43]

$$\begin{aligned} \text{MSE}(A) &= \text{Var}(A) + [\text{Bias}(A)]^2 \\ &\sim \left(1 + \frac{\partial \text{Bias}(A)}{\partial A} \right)^2 \frac{1}{F} + [\text{Bias}(A)]^2, \end{aligned} \quad (\text{E7})$$

and the proposed approach with the corrected FI and standard CRB ($\text{MSE} \sim 1/\tilde{F}$).

3. Fisher information regularization for dark objects

Regularization of FI for small A is performed according to Eq. (23) after substitution of Eq. (30):

$$\tilde{F}(A) = \max_{A'} \frac{K A'^{2(n-1)}}{\left(1 + |A' - A| \sqrt{K} A'^{n-1} \right)^2} \quad (\text{E8})$$

where $K = 4n^2 N \eta^n$. For $A' < A$ the derivative of the optimized expression is positive, i.e. the optimal A' is not less than A . For $A' > A$ the maximum of the optimized expression is reached at

$$A'_{\text{opt}} = \left(\frac{n-1}{\sqrt{K}} \right)^{1/n} \quad (\text{E9})$$

if $A \leq A'_{\text{opt}}$. Otherwise, the optimal value is $A' = A$ and no regularizing correction is applied.

4. Fisher information correction for the constraints

For the 1-parameter model, considered in Subsection IV A, the constraints to be taken into account by FI modification are $0 \leq A \leq 1$. The input FI is the result of regularization described in Appendix E 3. To avoid confusion with the final result of correction, we denote the input FI as F (not \tilde{F} as in Eq. (E8)). We follow the procedure from Subsection III B.

Both, the FIM F and the transformation matrix T have dimensions 1×1 in the considered case and represent just scalars: $T = \sqrt{F}$. The parameter transformation (for the first iteration) is $A' = \sqrt{F}(A - A^{(0)})$, where $A^{(0)}$ is the transmission amplitude value, for which FI is analyzed. Parameterization of the constraints in the form $a_j A \leq b_j$ is

$$A \leq 1 \Rightarrow a_1 = 1, b_1 = 1, \quad (\text{E10})$$

$$A \geq 0 \Rightarrow -A \leq 0 \Rightarrow a_0 = -1, b_0 = 0. \quad (\text{E11})$$

The transformed parameters of the constraints are

$$a'_1 = \frac{1}{\sqrt{F}}, b'_1 = 1 - A^{(0)}, a'_0 = -\frac{1}{\sqrt{F}}, b'_0 = A^{(0)}. \quad (\text{E12})$$

The local variable x , introduced in Appendix B, coincides with the transformed parameter up to the sign: $x = \pm A'$, where the “+” and “-” signs correspond to the constraint indices 1 and 0 respectively. The limiting values for the variable $x_0^{(j)} = b_j/|a_j|$ are equal to

$$x_0^{(1)} = \sqrt{F}(1 - A^{(0)}), x_0^{(0)} = \sqrt{F}A^{(0)}. \quad (\text{E13})$$

The probabilities P_1 and P_0 of the constraints violation are defined by Eq. (B2). For the model, discussed in Subsection IV A, the following relations hold for those probabilities:

$$P_1 \leq P_{\text{threshold}} \equiv 0.01 \text{ for } A \leq 0.937 \quad (\text{E14})$$

and

$$P_0 \leq P_{\text{threshold}} \text{ for } A \geq 0.242. \quad (\text{E15})$$

Therefore, for each A at most one of the constraints is active and requires application of the correction procedure. Due to the additivity of corrections applied to the same direction [53], one can avoid multiple iterations and reduce the constraint violation probability from its initial value to the target value P_{target} in one step.

The shrinking parameter ξ for the discussed correction step is prescribed by Eq. (B7) with $P'_j = P_{\text{target}}$. According to the last step of the correction procedure described in Subsection III B, the resulting corrected FI equals $\tilde{F} = (1 + \xi)F$, where F is the input FI (namely, the regularization result).

Appendix F: Visualization of Fisher information and covariance matrix for a 2-parameter model

Since FIM is a positive semi-definite matrix, it can serve as a quadratic form defining an ellipse in a 2-parameter case $\boldsymbol{\theta} = (\theta_1, \theta_2)$. The meaning of the ellipse is clearly seen from Eqs. (11) and (12) (see also Fig. 1 in Ref. [66] for illustration). If the estimation results are scattered according to multivariate normal distribution

$$p(\boldsymbol{\theta}) = \frac{\sqrt{\det \tilde{F}}}{2\pi} \exp \left[-\frac{1}{2} \Delta \boldsymbol{\theta}^T \tilde{F} \Delta \boldsymbol{\theta} \right], \quad \Delta \boldsymbol{\theta} = \boldsymbol{\theta} - \boldsymbol{\theta}_0, \quad (\text{F1})$$

centered at some point $\boldsymbol{\theta}_0$, the equation

$$\Delta \boldsymbol{\theta}^T \tilde{F} \Delta \boldsymbol{\theta} = 2 \log 2 \quad (\text{F2})$$

defines the boundary between the regions with $p(\boldsymbol{\theta}) > 1/2$ and $p(\boldsymbol{\theta}) < 1/2$. Moreover, each region will, in average, contain a half of the sampled results:

$$\int_{\Delta \boldsymbol{\theta}^T \tilde{F} \Delta \boldsymbol{\theta} \leq 2 \log 2} d^2 \boldsymbol{\theta} p(\boldsymbol{\theta}) = \frac{1}{2\pi} \int_{|\mathbf{r}| \leq 1} d^2 \mathbf{r} e^{-\mathbf{r}^2/2} = \frac{1}{2}. \quad (\text{F3})$$

Since CRB with standard FIM is valid for unbiased estimates, it is reasonable to take $\boldsymbol{\theta}_0$ equal to the true value of the parameters $\boldsymbol{\theta}$ for visualization of the standard FIM. The correction procedure (Subsection III B) shifts the probability distribution. Therefore, $\boldsymbol{\theta}_0$ should be taken as the center $\boldsymbol{\theta}^{(i_{\text{max}})}$ of the distribution after the last iteration (with the index i_{max}) for visualization of the corrected FIM \tilde{F} .

To visualize statistics of a set of randomly sampled points (in 2-dimensional space), one can assume a multivariate normal distribution based on the sample mean $\langle \boldsymbol{\theta} \rangle$ and covariance $C = \text{Cov}(\boldsymbol{\theta}, \boldsymbol{\theta})$:

$$p(\boldsymbol{\theta}) = \frac{1}{2\pi \sqrt{\det C}} \exp \left[-\frac{1}{2} \Delta \boldsymbol{\theta}^T C^{-1} \Delta \boldsymbol{\theta} \right], \quad \Delta \boldsymbol{\theta} = \boldsymbol{\theta} - \langle \boldsymbol{\theta} \rangle. \quad (\text{F4})$$

The quadratic form of the distribution corresponds to the ellipse defined by the equation

$$\Delta \boldsymbol{\theta}^T C^{-1} \Delta \boldsymbol{\theta} = 2 \log 2 \quad (\text{F5})$$

in the sense discussed above.

-
- [1] E. Abbe. Beiträge zur Theorie des Mikroskops und der mikroskopischen Wahrnehmung. *Archiv für mikroskopische Anatomie*, 9 (1): 413–468, 1873.
- [2] L. Rayleigh. XXXI. Investigations in optics, with special reference to the spectroscope. *The London, Edinburgh, and Dublin Philosophical Magazine and Journal of Science*, 8 (49): 261–274, 1879.
- [3] Kurt Rossmann. Point spread-function, line spread-function, and modulation transfer function: tools for the study of imaging systems. *Radiology*, 93 (2): 257–272, 1969.
- [4] Y. Shih. *An introduction to quantum optics: photon and biphoton physics*. CRC press, 2018.
- [5] Omar S. Magaña-Loaiza and Robert W. Boyd. Quantum imaging and information. *Reports on Progress in Physics*, 82 (12): 124401, 2019.
- [6] Lothar Schermelleh, Alexia Ferrand, Thomas Huser, Christian Eggeling, Markus Sauer, Oliver Biehlmaier, and Gregor P. C. Drummen. Super-resolution microscopy demystified. *Nature cell biology*, 21 (1): 72–84, 2019.
- [7] Kirti Prakash, Benedict Diederich, Rainer Heintzmann, and Lothar Schermelleh. Super-resolution microscopy: a brief history and new avenues. *Philosophical Transactions of the Royal Society A*, 380 (2220): 20210110, 2022.
- [8] V. Giovannetti, S. Lloyd, L. Maccone, and J. H. Shapiro. Sub-Rayleigh-diffraction-bound quantum imaging. *Physical Review A*, 79 (1): 013827, 2009.
- [9] D.-Q. Xu, X.-B. Song, H.-G. Li, D.-J. Zhang, H.-B. Wang, J. Xiong, and K. Wang. Experimental observation of sub-Rayleigh quantum imaging with a two-photon entangled source. *Applied Physics Letters*, 106 (17): 171104, 2015.
- [10] M. Unternährer, B. Bessire, L. Gasparini, M. Perenzoni, and A. Stefanov. Super-resolution quantum imaging at the Heisenberg limit. *Optica*, 5 (9): 1150–1154, 2018.
- [11] E. Toninelli, P.-A. Moreau, T. Gregory, A. Mihalyi, M. Edgar, N. Radwell, and M. Padgett. Resolution-enhanced quantum imaging by centroid estimation of biphotons. *Optica*, 6 (3): 347–353, 2019.
- [12] Thomas Dertinger, Ryan Colyer, Gopal Iyer, Shimon Weiss, and Jörg Enderlein. Fast, background-free, 3D super-resolution optical fluctuation imaging (SOFI). *Proceedings of the National Academy of Sciences*, 106 (52): 22287–22292, 2009.
- [13] Samuel T. Hess, Thanu P. K. Girirajan, and Michael D. Mason. Ultra-high resolution imaging by fluorescence photoactivation localization microscopy. *Biophysical journal*, 91 (11): 4258–4272, 2006.
- [14] Michael J. Rust, Mark Bates, and Xiaowei Zhuang. Subdiffraction-limit imaging by stochastic optical reconstruction microscopy (STORM). *Nature methods*, 3 (10): 793–796, 2006.
- [15] Joerg Schnitzbauer, Maximilian T. Strauss, Thomas Schlichthaerle, Florian Schueder, and Ralf Jungmann. Super-resolution microscopy with DNA-PAINT. *Nature protocols*, 12 (6): 1198–1228, 2017.
- [16] Min Gu, Yaoyu Cao, Stefania Castelletto, Betty Kouskousis, and Xiangping Li. Super-resolving single nitrogen vacancy centers within single nanodiamonds using a localization microscope. *Optics express*, 21 (15): 17639–17646, 2013.
- [17] Stefan W Hell and Jan Wichmann. Breaking the diffraction resolution limit by stimulated emission: stimulated-emission-depletion fluorescence microscopy. *Optics letters*, 19 (11): 780–782, 1994.
- [18] Stefan W. Hell and Matthias Kroug. Ground-state-depletion fluorescence microscopy: A concept for breaking the diffraction resolution limit. *Applied Physics B*, 60: 495–497, 1995.
- [19] P. C. Maurer, Jeronimo R. Maze, P. L. Stanwix, Liang Jiang, Alexey Vyacheslavovich Gorshkov, Alexander A Zibrov, Benjamin Harke, J. S. Hodges, Alexander S. Zibrov, Amir Yacoby, et al. Far-field optical imaging and manipulation of individual spins with nanoscale resolution. *Nature Physics*, 6 (11): 912–918, 2010.
- [20] R. A. Fisher. Theory of statistical estimation. In *Mathematical Proceedings of the Cambridge Philosophical Society*, volume 22, pages 700–725. Cambridge University Press, 1925.
- [21] H. Cramer. *Mathematical methods of statistics*. Princeton University Press, Princeton, 1946.
- [22] C. R. Rao. Information and accuracy attainable in the estimation of statistical parameters. *Bulletin of the Calcutta Mathematical Society*, 37: 81–91, 1945.
- [23] Sripad Ram, E. Sally Ward, and Raimund J. Ober. Beyond Rayleigh’s criterion: a resolution measure with application to single-molecule microscopy. *Proceedings of the National Academy of Sciences*, 103 (12): 4457–4462, 2006.
- [24] L. Motka, B. Stoklasa, M. D’Angelo, P. Facchi, A. Garuccio, Z. Hradil, S. Pascazio, F. V. Pepe, Y. S. Teo, J. Řeháček, et al. Optical resolution from fisher information. *The European Physical Journal Plus*, 131: 1–13, 2016.
- [25] Martin Paúr, Bohumil Stoklasa, Zdenek Hradil, Luis L Sánchez-Soto, and Jaroslav Rehacek. Achieving the ultimate optical resolution. *Optica*, 3 (10): 1144–1147, 2016.
- [26] J. Řeháček, Z. Hradil, B. Stoklasa, M. Paúr, J. Grover, A. Krzic, and L. L. Sánchez-Soto. Multiparameter quantum metrology of incoherent point sources: towards realistic superresolution. *Physical Review A*, 96 (6): 062107, 2017.
- [27] Yiyu Zhou, Jing Yang, Jeremy D. Hassett, Seyed Mohammad Hashemi Rafsanjani, Mohammad Mirhosseini, A. Nick Vamivakas, Andrew N. Jordan, Zhimin Shi, and Robert W. Boyd. Quantum-limited estimation of the axial separation of two incoherent point sources. *Optica*, 6 (5): 534–541, 2019.
- [28] A. B. Mikhalychev, B. Bessire, I. L. Karuseichyk, A. A. Sakovich, M. Unternährer, D. A. Lyakhov, Dominik L. Michels, André Stefanov, and D. Mogilevtsev. Efficiently reconstructing compound objects by quantum imaging with higher-order correlation functions. *Communications Physics*, 2 (1): 134, 2019.
- [29] Mankei Tsang, Ranjith Nair, and Xiao-Ming Lu. Quantum theory of superresolution for two incoherent optical point sources. *Physical Review X*, 6 (3): 031033, 2016.
- [30] Mankei Tsang. Subdiffraction incoherent optical imaging via spatial-mode demultiplexing. *New Journal of Physics*, 19 (2): 023054, 2017.
- [31] Martin Paúr, Bohumil Stoklasa, Jai Grover, Andrej Krzic, Luis L Sánchez-Soto, Zdeněk Hradil, and Jaroslav

- Řeháček. Tempering Rayleigh's curse with PSF shaping. *Optica*, 5 (10): 1177–1180, 2018.
- [32] M. Paúr, B. Stoklasa, D. Koutný, J. Řeháček, Z. Hradil, J. Grover, A. Krzic, and L. L. Sánchez-Soto. Reading out Fisher information from the zeros of the point spread function. *Optics Letters*, 44 (12): 3114–3117, 2019.
- [33] Yink Loong Len, Chandan Datta, Michał Parniak, and Konrad Banaszek. Resolution limits of spatial mode demultiplexing with noisy detection. *International Journal of Quantum Information*, 18 (01): 1941015, 2020.
- [34] A. B. Mikhalychev, P. I. Novik, I. L. Karuseichyk, D. A. Lyakhov, Dominik L. Michels, and D. S. Mogilevtsev. Lost photon enhances superresolution. *npj Quantum Information*, 7 (1): 125, 2021.
- [35] S. Vlasenko, A. B. Mikhalychev, I. L. Karuseichyk, D. A. Lyakhov, Dominik L. Michels, and D. Mogilevtsev. Optimal correlation order in superresolution optical fluctuation microscopy. *Physical Review A*, 102 (6): 063507, 2020.
- [36] Stanisław Kurdzialek and Rafał Demkowicz-Dobrzański. Super-resolution optical fluctuation imaging: fundamental estimation theory perspective. *Journal of Optics*, 23 (7): 075701, 2021.
- [37] Mankei Tsang. Conservative classical and quantum resolution limits for incoherent imaging. *Journal of Modern Optics*, 65 (11): 1385–1391, 2018.
- [38] H. L. Van Trees. *Detection, estimation, and modulation theory, part I: Detection, estimation, and filtering theory*. John Wiley and Sons Inc., 1968.
- [39] Petre Stoica and Randolph L. Moses. On biased estimators and the unbiased cramer-rao lower bound. *Signal Processing*, 21 (4): 349–350, 1990.
- [40] John D. Gorman and Alfred O. Hero. Lower bounds for parametric estimation with constraints. *IEEE Transactions on Information Theory*, 36 (6): 1285–1301, 1990.
- [41] Yonina C. Eldar. Rethinking biased estimation: Improving maximum likelihood and the cramer-rao bound. *Foundations and Trends® in Signal Processing*, 1 (4): 305–449, 2008.
- [42] James O. Berger. On the inadmissibility of unbiased estimators. *Statistics & Probability Letters*, 9 (5): 381–384, 1990.
- [43] Yonina C. Eldar. Minimum variance in biased estimation: Bounds and asymptotically optimal estimators. *IEEE Transactions on Signal Processing*, 52 (7): 1915–1930, 2004.
- [44] Zvika Ben-Haim and Yonina C. Eldar. A lower bound on the bayesian mse based on the optimal bias function. *IEEE Transactions on Information Theory*, 55 (11): 5179–5196, 2009.
- [45] Alfred O. Hero, Jeffrey A. Fessler, and Mohammad Usman. Exploring estimator bias-variance tradeoffs using the uniform cr bound. *IEEE Transactions on Signal Processing*, 44 (8): 2026–2041, 1996.
- [46] C. H. Hua, N. H. Clinthorne, S. J. Wilderman, J. W. LeBlanc, and W. L. Rogers. Quantitative evaluation of information loss for compton cameras. *IEEE Transactions on Nuclear Science*, 46 (3): 587–593, 1999.
- [47] Yonina C. Eldar. Uniformly improving the cramer-rao bound and maximum-likelihood estimation. *IEEE Transactions on Signal Processing*, 54 (8): 2943–2956, 2006.
- [48] L. J. Meng and Neal H. Clinthorne. A modified uniform cramer-rao bound for multiple pinhole aperture design. *IEEE transactions on medical imaging*, 23 (7): 896–902, 2004.
- [49] L. J. Meng, N. H. Clinthorne, S. Skinner, R. V. Hay, and M. Gross. Design and feasibility study of a single photon emission microscope system for small animal i-125 imaging. *IEEE transactions on nuclear science*, 53 (3): 1168–1178, 2006.
- [50] Ling-Jian Meng and Nan Li. A vector uniform cramer-rao bound for spect system design. In *2008 IEEE Nuclear Science Symposium Conference Record*, pages 4054–4064. IEEE, 2008.
- [51] E. T. Jaynes. *Probability theory: the logic of science*. Washington University St. Louis, MO, 1996.
- [52] M. Vallisneri. Use and abuse of the Fisher information matrix in the assessment of gravitational-wave parameter-estimation prospects. *Physical Review D*, 77 (4): 042001, 2008.
- [53] Alexander Mikhalychev, Dmitri Mogilevtsev, Yong Siah Teo, Jaroslav Řeháček, and Zdeněk Hradil. Bayesian recursive data-pattern tomography. *Physical Review A*, 92 (5): 052106, 2015.
- [54] E. L. Lehmann and G. Casella. *Theory of point estimation*. Springer Science & Business Media, 1998.
- [55] K.-R. Koch. *Introduction to Bayesian statistics*. Springer Science & Business Media, 2007.
- [56] C. W. Helstrom. Quantum detection and estimation theory. *Journal of Statistical Physics*, 1 (2): 231–252, 1969.
- [57] Alexander S. Holevo. *Probabilistic and statistical aspects of quantum theory*, volume 1. North-Holland Publishing Company, 1982.
- [58] Matteo G. A. Paris. Quantum estimation for quantum technology. *International Journal of Quantum Information*, 7 (supp01): 125–137, 2009.
- [59] Mankei Tsang. Quantum limits to optical point-source localization. *Optica*, 2 (7): 646–653, 2015.
- [60] Ranjith Nair and Mankei Tsang. Far-field superresolution of thermal electromagnetic sources at the quantum limit. *Physical review letters*, 117 (19): 190801, 2016.
- [61] Zachary Dutton, Ronan Kerviche, Amit Ashok, and Saikat Guha. Attaining the quantum limit of superresolution in imaging an object's length via predetection spatial-mode sorting. *Physical Review A*, 99 (3): 033847, 2019.
- [62] Rafał Demkowicz-Dobrzański, Wojciech Górecki, and Mădălin Guță. Multi-parameter estimation beyond quantum fisher information. *Journal of Physics A: Mathematical and Theoretical*, 53 (36): 363001, 2020.
- [63] Cosmo Lupo, Zixin Huang, and Pieter Kok. Quantum limits to incoherent imaging are achieved by linear interferometry. *Physical Review Letters*, 124 (8): 080503, 2020.
- [64] Sisi Zhou and Liang Jiang. Modern description of Rayleigh's criterion. *Physical Review A*, 99 (1): 013808, 2019.
- [65] Evangelia Bisketzi, Dominic Branford, and Animesh Datta. Quantum limits of localisation microscopy. *New Journal of Physics*, 21 (12): 123032, 2019.
- [66] Alexander Mikhalychev, Konstantin Zhevno, Svetlana Vlasenko, Andrei Benediktovitch, Tatjana Ulyanenkova, and Alex Ulyanekov. Fisher information for optimal planning of X-ray diffraction experiments. *Journal of Applied Crystallography*, 54 (6): 1676–1697, 2021.
- [67] Gabriela Barreto Lemos, Victoria Borish, Garrett D. Cole, Sven Ramelow, Radek Lapkiewicz, and Anton Zeilinger. Quantum imaging with undetected photons.

- Nature*, 512 (7515): 409–412, 2014.
- [68] A. A. Pushkina, G. Maltese, J. I. Costa-Filho, P. Patel, and A. I. Lvovsky. Superresolution linear optical imaging in the far field. *Physical Review Letters*, 127 (25): 253602, 2021.
- [69] J. Kiefer. Optimum experimental designs. *Journal of the Royal Statistical Society: Series B (Methodological)*, 21 (2): 272–304, 1959.
- [70] S. P. Asprey and S. Macchietto. Designing robust optimal dynamic experiments. *Journal of Process Control*, 12 (4): 545–556, 2002.
- [71] J. R. Banga, K. J. Versyck, and J. F. Van Impe. Computation of optimal identification experiments for nonlinear dynamic process models: a stochastic global optimization approach. *Industrial & Engineering Chemistry Research*, 41 (10): 2425–2430, 2002.
- [72] D. Faller, U. Klingmüller, and J. Timmer. Simulation methods for optimal experimental design in systems biology. *Simulation*, 79 (12): 717–725, 2003.
- [73] Ilya Karuseichyk, Giacomo Sorelli, Mattia Walschaers, Nicolas Treps, and Manuel Gessner. Resolving mutually-coherent point sources of light with arbitrary statistics. *Physical Review Research*, 4 (4): 043010, 2022.
- [74] Clémentine Rouvière, David Barral, Antonin Grateau, Ilya Karuseichyk, Giacomo Sorelli, Mattia Walschaers, and Nicolas Treps. Ultra-sensitive separation estimation of optical sources. *Optica*, 11 (2): 166–170, 2024.
- [75] I. N. Agafonov, M. V. Chekhova, T. Sh. Iskhakov, and L.-A. Wu. High-visibility intensity interference and ghost imaging with pseudo-thermal light. *J. Mod. Opt.*, 56 (2-3): 422–431, 2009.
- [76] X.-H. Chen, I. N. Agafonov, K.-H. Luo, Q. Liu, R. Xian, M. V. Chekhova, and L.-A. Wu. Arbitrary-order lensless ghost imaging with thermal light. *Opt. Lett.*, 35 (8): 1166, 2010.
- [77] P.-A. Moreau, E. Toninelli, P. A. Morris, R. S. Aspden, T. Gregory, G. Spalding, R. W. Boyd, and M. J. Padgett. Resolution limits of quantum ghost imaging. *Opt. Express*, 26 (6): 7528, 2018. doi:10.1364/OE.26.007528.